1976

The interaction of nitric oxide with the (1010) face of ruthenium

Thomas William Orent
Iowa State University

The interaction of nitric oxide with the $(10\bar{1}0)$ face of ruthenium

by

Thomas William Orent

A Dissertation Submitted to the

Graduate Faculty in Partial Fulfillment of

The Requirements for the Degree of

DOCTOR OF PHILOSOPHY

Department: Chemistry
Major: Physical Chemistry

Approved:

Signature was redacted for privacy.

In Charge of Major Work

Signature was redacted for privacy.

For the Major Department

Signature was redacted for privacy.

For the Graduate College

Iowa State University
Ames, Iowa

1976

TABLE OF CONTENTS

	Page
INTRODUCTION	1
AUGER ELECTRON SPECTROSCOPY	3
Historical Development	3
The Secondary-Electron Energy Distribution	6
Technique of Obtaining Electron-Excited Auger Electron Spectra	8
Interpretation of Auger Spectra	12
Characteristic energy	12
Chemical shifts	15
Line shape	17
Intensity	19
LOW-ENERGY ELECTRON DIFFRACTION	25
REVIEW OF PREVIOUS RESEARCH ON THE INTERACTION OF NITRIC OXIDE WITH RUTHENIUM	30
EXPERIMENTAL	37
Purpose of Experiments	37
Experimental Apparatus	39
Auger Spectrometer	40
RESULTS	45
The Clean Surface	45
LEED Pattern from Clean Ru(10$\bar{1}$0) Surface	52

Page

Auger Analysis of Adsorbed Gases 54

LEED and Auger Electron Spectroscopy Results 58

DISCUSSION OF RESULTS 70

Structures Resulting from the Interaction of Nitric Oxide and Oxygen with Ru(10$\bar{1}$0) 70

The Relationship Between the Observed Structures and the Results of Previous Investigations 91

FUTURE INVESTIGATIONS 94

BIBLIOGRAPHY 95

INTRODUCTION

The reduction of nitric oxide became a topic of great interest in catalytic chemistry when the Clean Air Act of 1970 called for the effective removal of nitric oxide from automobile exhaust. The catalytic properties of supported ruthenium for this reaction have been found to be unique among the noble metals. Most noble metals catalyze the reduction of nitric oxide in the presence of hydrogen and carbon monoxide, but many produce various amounts of nitrous oxide and ammonia which are undesirable from an environmental point of view. Only ruthenium stands out as a metal which produces mainly nitrogen (1-6).

Efforts to characterize highly idealized gas-solid reaction systems by various methods under ultrahigh vacuum conditions are motivated by the philosophy that "real" catalytic systems, while too complex to be described, can be manipulated in a qualitatively predictable fashion on the basis of insight achieved from the quantitative description of the properties of well-characterized if simpler systems. It is widely believed that the determination of the geometrical and electronic structure of chemisorbed intermediates and the systematic relating of this structure to the catalytic activity comprise the main ingredient in establishing models of catalytic reactions with predictive capability. Studies of the interactions of small gaseous molecules with clean surfaces are the bases of catalytic studies, but despite the practical importance

of ruthenium catalysts, relatively few such studies have been performed (7-11).

The purpose of this investigation was to employ the low-energy electron diffraction (LEED) technique to probe the atomic geometry of the surfaces that resulted from the steady-state interaction of nitric oxide with Ru(10$\bar{1}$0) as a function of temperature and pressure and Auger electron spectroscopy (AES) to identify the atomic species present on these surfaces. Results were obtained at reactant partial pressures in the range from 10^{-9} to 10^{-6} torr and substrate temperatures from -25 to 950° C. The interaction of molecular oxygen with the surface was also examined. A qualitative correlation exists between the observed structures and the reported enhancement in the catalytic activity of supported ruthenium after the catalyst had been pretreated with oxygen (2-4, 6).

AUGER ELECTRON SPECTROSCOPY

Historical Development

In 1925 Pierre Auger (12) published a paper reporting the observation of "tertiary electrons" in a Wilson cloud chamber during the excitation of photoelectrons from noble gas atoms by monoenergetic x rays. These "tertiary" or Auger electrons originated from the same atoms as the photoelectrons, had an isotropic distribution and were emitted with energies characteristic of the atom from which they originated, independent of the energy of the x rays. Auger, interpreting the origin of these electrons in terms of the Bohr model of the atom, postulated the existence of a completely new mechanism for energy exchange between electrons and radiation. The Auger electron received its energy in a radiationless transfer from an outer shell electron which dropped to the core level vacancy left by the ejected photoelectron. The transferred energy is roughly the difference in energy between the two levels involved and thus characteristic of the atom. An atom ionized in a core shell can relax by either emission of an x ray or by the Auger process. His results provided confirmatory evidence for the Bohr model.

The first theoretical calculations on the Auger effect were performed by Wentzel (13) in 1927. He computed the nonrelativistic Auger transition rate using first-order, time-dependent perturbation theory with the

Coulomb interaction between two electrons regarded as the perturbation. The same transition rate has been obtained by regarding the phenomenon as an internal absorption of radiation. In the relativistic limit, the only method available for handling the problem is to consider the electromagnetic field created by the transition of the first electron as the perturbation; however, the nonrelativistic form of this rate expression is identical to the radiationless-transition model rate. It is immaterial whether the phenomenon is regarded as internal conversion of a photon or the result of direct interaction between electrons.

The theoretical Auger transition rate at this level of approximation is independent of the nuclear charge, Z; and the x ray emission rate varies as Z^4. As a result, Auger emission is favored over x ray emission for low Z elements. Estimated values of the K-shell Auger yield range from 0.9917 for oxygen to 0.0325 for uranium. Early interest in the Auger effect was aimed at explaining the variations in x ray fluorescence yields. The role of the Auger effect in atomic, nuclear and elementary particle physics has been reviewed (14, 15).

The exploitation of the Auger electron's energy being very precisely characteristic of the parent atom for material analysis was hampered by the lack of high vacuum and electronic techniques necessary for measuring electron energies. The first work on electron-excited Auger spectroscopy was reported by J. J. Lander (16) in 1953. Using an

electrostatic sector analyzer, he observed Auger peaks of a number of metals and oxygen and changes in the spectrum due to oxidation. He estimated the escape depth of Auger electrons from a surface at ten atomic layers. Lander concluded that the method offered a positive means of analysis where the material of interest was present to a depth of several atomic layers and the high vacuum condition was not prohibitive.

This interesting technique for surface analysis was not immediately capitalized upon since the secondary-electron emission from an electron bombarded surface contains much more information than just Auger currents. The extraction of small Auger signals from a very much larger background was a problem. This problem was finally solved by L. A. Harris (17) in 1967. He used an instrument similar to that used by Lander (16), but he electronically differentiated the secondary emission spectrum which enhanced the Auger features. The method of differentiating with respect to energy permitted significant noise reduction and increased signal gain. Shortly thereafter Weber and Peria (18) obtained the same type of spectra from a low-energy electron diffraction (LEED) apparatus by taking second derivatives of the collected current. Their demonstration that Auger spectroscopy could be done in existing apparatus already in the hands of workers vitally interested in surface studies insured its immediate use and rapid improvement. One

of the major advances in technique was the application of the cylindrical mirror analyzer (19). The instrument has high transmission and high energy resolution thus permitting rapid analysis with low electron currents.

The Secondary-Electron Energy Distribution

Auger electrons are found among the various secondary electrons ejected into the vacuum under the influence of a beam of incident electrons of energy E_o. In order to observe the Auger electrons, it is necessary to measure the electron energy distribution, N(E). A typical N(E) versus E curve is shown in Fig. 1. Three major features

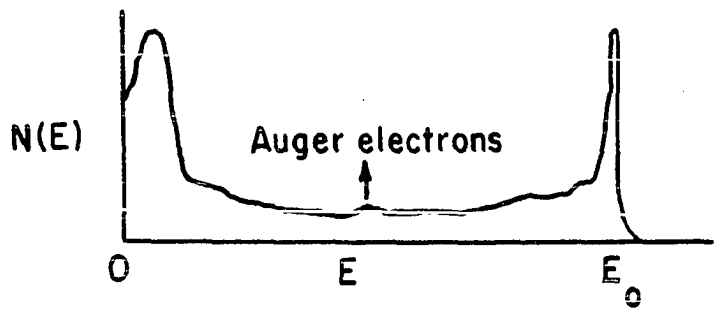

Fig. 1. Typical secondary electron energy distribution, N(E), of a solid produced by a primary electron beam of energy E_o. Auger electrons appear as small bumps.

are visible: (1) a sharp peak at the incidence energy E_o due to elastically reflected primaries, (2) a large peak near $E = 0$ and (3) an intermediate energy region with relatively few electrons. The relative intensities of the various features can be understood by examining the nature and magnitude of the elemental scattering processes experienced by the incident electrons.

The incident electrons can interact with the valence electrons in the solid. The electrons can lose energy to bulk as well as surface plasmons and to other types of excitation of the valence electron fluid like single particle intraband and interband transitions. The valence electrons in the solid which are excited by the incident electrons often have sufficient energy to escape into the vacuum. The "true secondary" peak near $E = 0$ results from the cascade-loss processes of the incident electrons which create a large population of low-energy ($E < 25$ eV) electrons. Inelastic total scattering cross sections for a 10 eV energy loss for $E_o = 1000$ eV are on the order of 10^{-18} cm^2 (20).

The elastic peak at $E = E_o$ is caused by the back scattering of the incident electrons from the ion cores in the solid. It is the intensity and angular dependence of this peak which is measured in LEED. Electron-ion core elastic scattering total cross sections are on the order of 10^{-16} cm^2.

Incident electrons can create core holes in the atomic constituents

of the solid. This interaction produces an ion of energy E_i, where E_i is the binding energy of the core electron, and two electrons the sum of whose energies is $E_o - E_i$. The ejected core electrons produce an ionization edge in N(E). The core holes can be filled by the Auger process, but the number of Auger electrons is very small because the maximum probability of creating a core hole scales roughly as E_i^{-2} (cross sections on the order of 10^{-20} cm^2) and this probability is further attenuated by the possibility of x ray fluoresence.

Technique of Obtaining Electron-Excited Auger Electron Spectra

The initial ionization of core electrons required for the Auger process is accomplished by bombarding a solid in ultrahigh vacuum with high energy electrons. The electrons emitted from the sample are collected, and their energy distribution is determined by an energy analyzer. A variety of energy analyzers are presently in use, but only the retarding potential analyzer will be discussed. A generalized analyzer and its associated electronic components are shown in Fig. 2. This analyzer has two retarding grids which are connected together and which are shielded from the sample and the collector by grounded grids. The retarding potential applied to these grids is slowly swept through the range 0 to $-V_o$ where $e|V_o| = E_o$, the energy of the incident electrons. The total current collected when a potential V' is applied to the retarding grids consists of all electrons with kinetic energy greater than

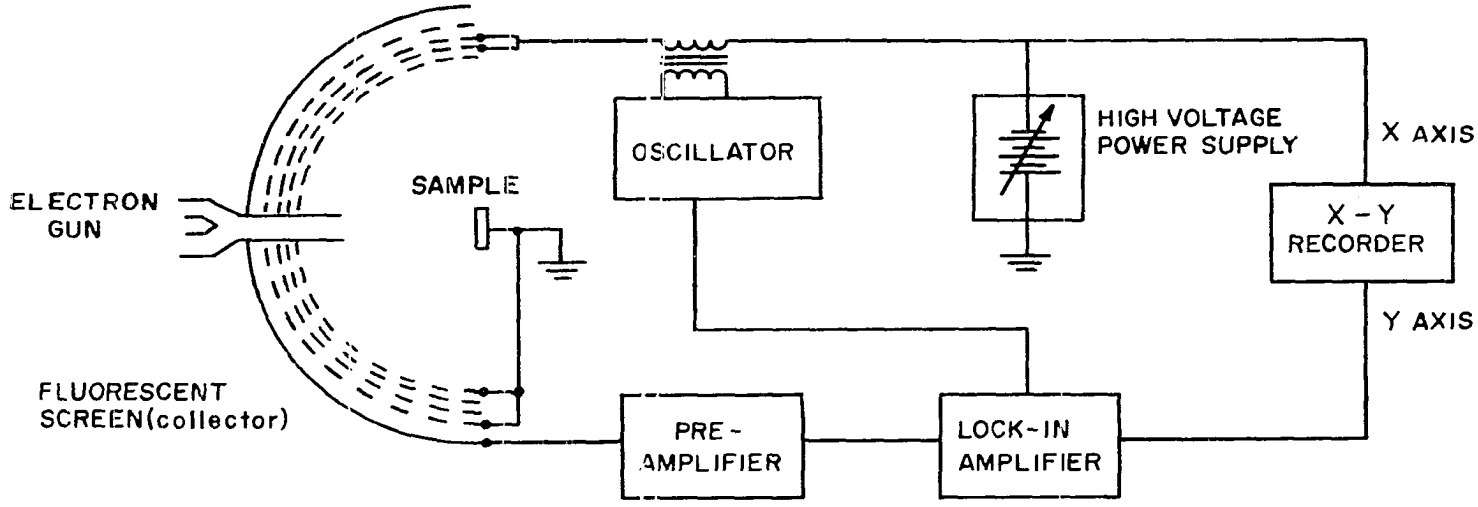

Fig. 2. General electronic circuit arrangement for Auger electron spectroscopy using hemispherical electron optics.

$E' = e|V' + \phi_{spec}|$ (see Fig. 3) and is given by the integral:

$$I(E', E_o) = \int_{E'}^{E_o} N(E)dE \quad . \qquad (1)$$

Consequently N(E) can be obtained by taking the first derivative of the collected current. Auger electron currents in $I(E', E_o)$ occur at fixed energy values characteristic of the parent atom. Changes in the primary beam energy do not alter the energy values; although such changes may alter the intensities of the Auger currents due to associated variations in ionization cross sections.

In practice the collected current is electronically differentiated by external curcuits. The first step in this process, which was first used by Leder and Simpson (21) in 1958 and which has come to be known as potential modulation differentiation, is to superimpose a low level ac modulating signal upon the dc potential applied to the retarding grids. This signal is supplied by the oscillator and is of the form $k\sin\omega t$. Provided that $k << e|V'|$, the collected current may be represented by a Taylor series expansion:

$$I(E') = I_o + \left(\frac{dI}{dE}\right)_{E'} k\sin\omega t + \left(\frac{d^2I}{dE^2}\right)_{E'} \frac{k^2}{4}(1 + \cos 2\omega t) + \cdots \quad . \qquad (2)$$

The first derivative of the collected current is the coefficient of the leading term in the series expression for the ac component with frequency ω. The rate of convergence of this series can be adjusted and the leading term emphasized by using a sufficiently small modulation amplitude k.

Taylor (22) has analyzed this problem for the case of N(E) given by a Gaussian function. As the modulation amplitude increases, the amplitude of the fundamental ac signal becomes increasingly less than proportional to the coefficient of the leading term, kN(E). The error is approximately 14% when the peak-to-peak amplitude is equal to the full width at half-height of the Gaussian peak. Similarly the amplitude of the second harmonic signal is slightly less than proportional to the coefficient of the second term in Eq. (2). The error is almost 20% for a peak-to-peak amplitude equal to the full width at half-height.

It is the function of the preamplifier and the lock-in amplifier to detect and amplify the selected ac component. In order to obtain N(E), the input circuit of the preamplifier is tuned to ω. The total output consists of a signal that is strictly proportional to the ac signal at the input, and this signal is fed to one channel of the lock-in amplifier. The lock-in amplifier performs synchronous or in-phase detection and amplification by comparing the phase of the signal from the preamplifier to the phase of the oscillator signal which is supplied to the reference channel. As a result, only that portion of the collected current which is in phase with the ac signal on the retarding grids is detected and amplified, i.e., only those electrons with kinetic energies near $e|V'|$ are counted by the external circuitry. The output of the lock-in amplifier is fed to the Y axis of a recording device, and the X axis is

driven by a dc potential proportional to V'. The resulting X-Y plot is proportional to the secondary electron energy distribution.

The Auger current at a particular energy E has to compete with the fluctuation or shot noise (the statistical noise associated with the measurement of discrete particles) from all electrons capable of overcoming the retarding voltage. This leads to rather poor signal-to-noise characteristics, which limits the speed at which the spectrum can be generated. To enhance the weak but relatively sharp features associated with the Auger electrons, the higher frequency spectral components of the collected current are amplified selectively by measuring its second derivative with respect to energy. The background is suppressed since it is a relatively slowly varying function of energy as compared to the Auger features. The second derivative spectrum is obtained by tuning the phase-sensitive detector to 2ω. An Auger feature in a $dN(E)/dE$ versus E plot is characterized by prominent positive and negative peaks.

Interpretation of Auger Spectra

Characteristic energy

An energy level diagram of Auger electron emission for a core level valence-valence transition is shown in Fig. 3. The kinetic energy of the ejected electron depends on the positions of the core hole and of the two valence band holes. If the core hole recombination is with an electron in a state of energy ϵ_1 in the valence band and the Auger electron is

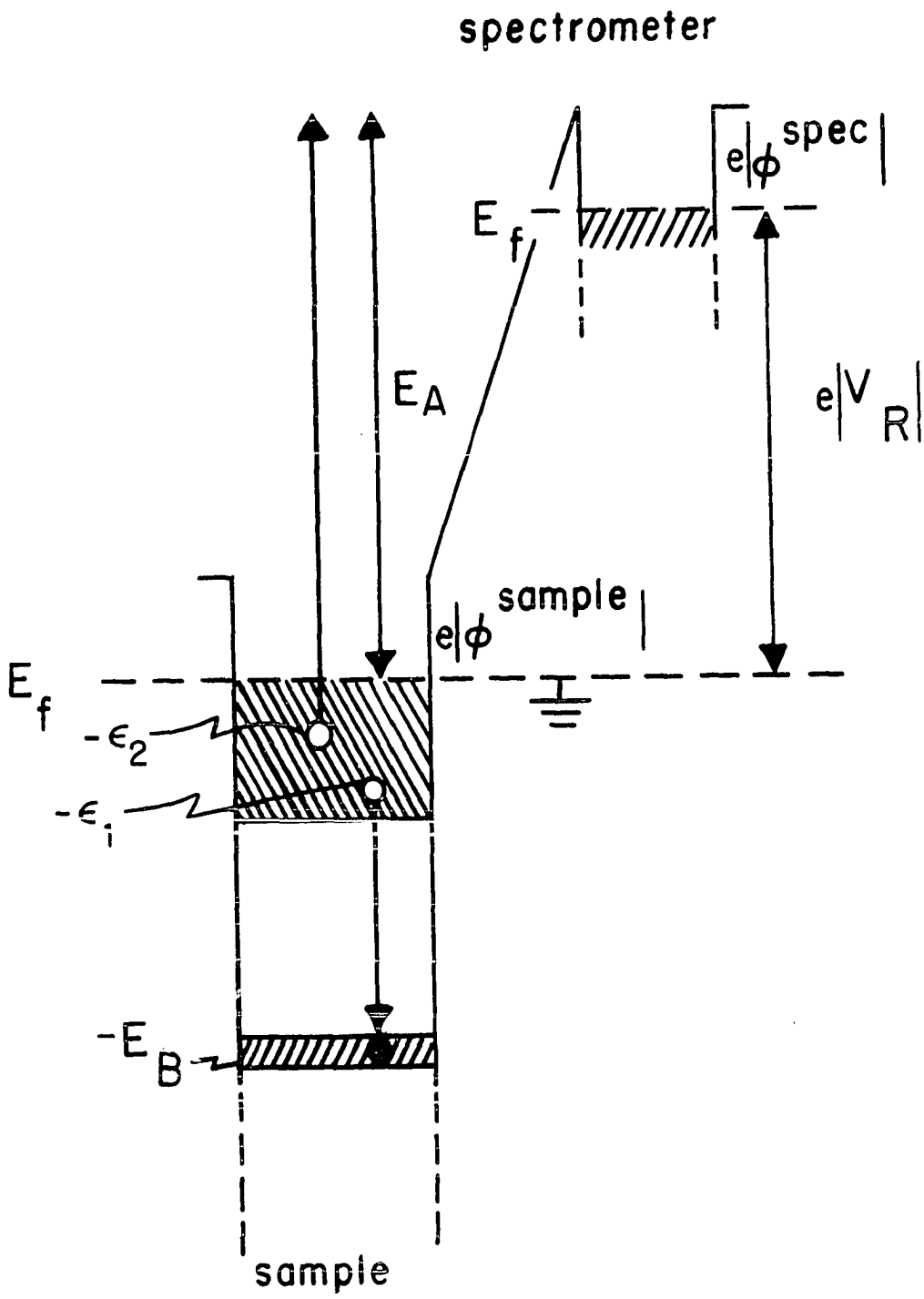

Fig. 3. Energy level diagram of Auger electron emission. The initial state includes a vacancy in a core level of binding energy E_B. All energies are relative to the grounded Fermi level of the sample.

ejected from a state ϵ_2, also in the valence band, then the energy E_A of the Auger electron relative to the grounded Fermi level of the sample is:

$$E_A = E_B - \epsilon_1 - \epsilon_2 \quad . \tag{3}$$

In the measurement of the characteristic energy with a retarding potential analyzer, the characteristic energy E_A is equated to the retarding potential plus the analyzer work function:

$$E_A = e\left|V_R + \phi_{spec}\right| \quad . \tag{4}$$

A typical Auger peak in a second-derivative spectrum has a large negative peak, an associated positive peak and possibly neighboring fine structure. The negative part is almost always expected to be sharp and prominent, and for this reason most workers have adopted the convention of assigning the energy of the minimum of the negative portion to that Auger transition.

Auger energies are almost universally designated in terms of an WXY notation where the letters are the x ray nomenclature for the energy levels of the ionized core electron, the electron which fills the core hole and the ejected electron respectively. For example, a Ru $M_5N_3N_5$ Auger transition would be produced by the removal of an electron from the M_5 level, the filling of this hole by an electron from the N_3 level, followed by the ejection of an electron from the N_5 level.

The energy difference $E_B - \epsilon_1$ can be found in x ray and photoelectron

energy tables, but the energy ϵ_2 is not known since, after Auger ejection, the system is doubly ionized and x ray energy levels do not adequately describe the allowed final states of the system. The kinetic energy can be semiempirically estimated by assuming that ϵ_2 should be approximately equal to the single-ionization energy for the corresponding level of the next heavier element:

$$\epsilon_2(Z) = \epsilon_2(Z + \Delta) \qquad (5)$$

where Z is the atomic number and Δ has been found empirically to be between 0.5 and 1.0. A discussion of the methods employed to theoretically calculate Auger energies can be found in a recent review by Chang (23).

For a heavy element the L-shell Auger spectrum alone consists of hundreds of lines, the energies of which are not susceptible to precise first-principle calculations. Serious ambiguities arise in the identification of Auger transitions for all but the lightest elements. Elemental identification is generally based on matching spectra against "standard" plots taken from samples of known composition.

Chemical shifts

There have been numerous reports of shifts in the positions of Auger peaks with changes in the chemical environment of the atom. Shifts in energy of atomic levels due to environmental conditions of the parent atom are known as "chemical shifts." These shifts can be caused by

changes in the valence band density of states or by core level shifts caused by a net exchange of electrons among atoms in a solid (24).

Chemical shifts are difficult to measure and interpret using Auger spectra. They are often small (≤ 1 eV) and cannot be accurately measured using the relatively broad Auger peaks. Since the observed energy of an Auger electron depends on the binding energies of three levels, any or all of them may be shifted. As a result, if Δ_W, Δ_X and Δ_Y (where Δ_Y is the shift in the doubly ionized state) are the chemical shifts of the W, X and Y levels, the Auger peak will be shifted by:

$$\Delta E = \Delta_W - \Delta_X - \Delta_Y \quad . \qquad (6)$$

Since only ΔE is measured, the individual Δ_i are not known.

Peak shifts observed in Auger spectra may serve to characterize differences in chemical environment even though they do not yield readily to quantitative analysis. Wagner (25) has proposed the use of an Auger parameter, α, defined as the difference in kinetic energy between an Auger line and a photoelectron line. This quantity is unique for each compound and can be measured more accurately than absolute line positions. Data on sodium showed a total spread in α of 9.6 eV between isolated Na atoms and Na metal with the Na salts occupying a 3.4 eV range precisely in the center.

Line shape

Auger electron spectra from free atoms reveal inherent Lorentzian line shapes due to the natural widths of the initial and final states. Auger spectra from solid surfaces are more complex due to band structure effects. The line shape for a core level valence-valence transition is related to the density of valence band states. The energy distribution of Auger electrons must take into account all possible combinations of energies ϵ_1 and ϵ_2 (see Fig. 3) allowed by the conservation of energy, as expressed in Eq. (3). The transition density $T(E_A)$ is given, in this simple picture, by the self-convolution of the valence band density of states:

$$T(E_A) = \int_0^E N_v(E')N_v(E - E')\,dE' \qquad (7)$$

where

$$E = \epsilon_1 + \epsilon_2 = E_B - E_A \quad . \qquad (8)$$

This expression will be broadened by the energy width of the core level which is a consequence of the finite lifetime τ of the core hole. From the uncertainty principal the width is $\hbar/\tau$; as a result, the initial core level must be described by a state distribution function which has the form of a Lorentzian. For the narrowest core levels, the energy corresponding to this finite lifetime is about 0.2 eV. The width of a core level valence valence Auger line is twice the occupied width of the valence band.

Typical Auger lines are from 3 to 20 eV wide.

Since the valence band is sensitive to the chemical environment of an atom, any redistribution of electrons due to differences in the bonding may be reflected in a change in the shape of the Auger peak. Auger spectra for atoms in different chemical environments may serve as characteristic "fingerprints" of the type of chemical bonding. Haas, Grant and Dooley (26) observed changes in the line shape of the carbon peak in second-derivative spectra among CO on W(112), W_2C, graphite and diamond. Hooker and Grant (27,28) compared the Auger spectra of gaseous CO and CO adsorbed on Ni(110) and found similarities between the oxygen peaks which they concluded indicated weak bonding of nondissociated CO to the surface. Changes in line shape with chemical environment have also been reported for silicon and sulphur (23).

The measured Auger line shape differs from the "actual" line shape due to the cumulative effects of finite instrument resolution plus inelastic scattering. Energy losses to single electron and plasmon excitations will spread the Auger electrons over a range of energies usually producing a broad satellite peak centered some 10 to 20 eV below the parent peak. A fundamental problem in line shape analysis is the effect of the instrument on the recorded data. The degrading effect of the instrument can be treated analytically through the use of an instrument broadening function. A measured spectrum, $S(x)_{meas}$, can be written

as the convolution product of the "actual" spectrum, S(x), with the instrument response:

$$S(x)_{meas} = S(x)*T(x) \qquad (9)$$

where T(x) is the function the instrument would record for a hypothetical signal in the form of a Dirac delta function.

When the potential modulation method is used to obtain a derivative spectrum, the instrument response function depends on the amplitude of the oscillation. Park and Houston (29) have derived analytical expressions for the broadening functions for the first and second derivative spectra obtained with retarding grid analyzers. These functions do not include the effect of the finite analyzer window. Mularie and Peria (30) have shown that the elastically scattered peak and its associated characteristic loss features provide a satisfactory instrument response function to correct for both the instrument and inelastic interactions.

Intensity

The Auger current, $i_A(E_o)$, per unit area of sample arising from incident electrons of energy E_o will bear the approximate proportional relationship:

$$i_A(E_o) \propto i(E_o)\sigma(E_o, E_B)\gamma(E_A)\tau(E_A) \qquad (10)$$

where $i(E_o)$ is the incident flux of electrons, $\sigma(E_o, E_B)$ is the cross section for inner shell ionization of the appropriate level (binding energy

E_B), $\gamma(E_A)$ is the probability that an excited atom will decay through an Auger transition of energy E_A and $\tau(E_A)$ is the effective number of layers of the solid contributing to the Auger current. The product notation is only symbolic because each factor is not independent of the others but is a complicated function of many variables. The effect of the analyzer, e.g., geometry of the analyzer aperature, the transmission and the detector sensitivity, has not been explicitly included.

Determination of the effective ionization current is very difficult since not only incident primary electrons but also backscattered primary electrons produce ionization events. Both elastically and inelastically scattered primaries can contribute to the ionization frequency as long as their energies exceed E_B. The energy distribution of backscattered primaries, while in the solid and prior to their last potential ionization event, is unknown, but these electrons may produce up to half of the Auger intensity. The backscattered contributions to the Auger yields for pure silicon and silver have been measured by Gallon (31) by an iterative procedure which took account of the measured energy dependence of the Auger yield and the measured energy distribution of escaping backscattered electrons. He found the backscattered contributions were 30% for silver and 20% for silicon. The backscattering factor is a function of both atomic number and primary beam energy. Calculations by Bishop and Riviere (32) predict a nearly linear increase in the backscattering

factor with increasing atomic number up to about Z = 30. They also show a monotonic increase in this factor with increasing incident electron energy. Up to 50% of the Auger yield may be produced by backscattered electrons for heavy elements (Z > 30) and E_o/E_A equal to ten.

The electron impact ionization cross section, $\sigma(E_o, E_B)$, can be characterized in the following manner. As the primary beam energy is increased from zero, the cross section remains zero until the beam energy reaches the binding energy of the level in question. Above $E_o/E_B = 1$ the calculations of Bishop and Riviere (32) show that the cross section should increase very rapidly to a maximum near $E_o/E_B \approx 3$ and then begin to decrease very slowly. However, primary electrons create secondaries, some of which have $E > E_B$, and which can cause further ionization events. These secondaries increase up to a point with increasing E_o; and this factor increases the ionization probability. The maximum ionization probability has been observed experimentally to occur near $E_o/E_B \approx 6$. Since core level ionizations are atomic in nature, ionization cross sections for a given element subshell should be constant, irrespective of the chemical environment of the element.

Following the ionization event, two processes compete in the de-excitation scheme: Auger electron emission and x ray fluorescence. The trend is to heavily favor the Auger process in events involving core level binding energies less than a few kilovolts (15). Since Auger

transitions can occur through several possible channels after ionization of a particular core level, the proportion of the total current in each peak must be determined.

The most important factor relating the Auger current to the population density of a particular element is $\tau(E_A)$, the effective number of layers of a solid contributing to the Auger current. Only those ejected electrons which do not lose energy by inelastic scattering on their way to the surface will appear in the spectrum at their original characteristic positions. Electron-electron interactions result in strong inelastic-collision-induced attenuation of the Auger electron intensity. The surface sensitivity of Auger electron spectroscopy is due to this inelastic collision damping. The magnitude of this damping is a function of the material and the energy of the Auger electron and is independent of the primary beam energy.

The attenuation of Auger electron intensities due to inelastic scattering of the escaping electrons is generally treated as having an exponential dependence on material thickness. As a result, the effective sampling depth can be parameterized in terms of the single variable $\lambda(E_A)$, the escape depth, which is the path length for which an electron with energy E_A has a probability equal to $1 - e^{-1}$ of being inelastically scattered. Escape depths have been estimated empirically by noting the attenuation of a characteristic substrate Auger signal as an overlayer of a particular

material is made to increase in thickness. Brundle (33) has tabulated many of the experimental determinations of $\lambda(E_A)$. Generally the escape depth has been observed to have a minimum of a few angstroms near 100 eV and to increase approximately as $E^{\frac{1}{2}}$ from 100 to 2000 eV. A more complete discussion of escape depths can be found in a review by Powell (34).

The lack of quantitative information regarding fundamental mechanisms involved in the production of Auger electrons and about experimental factors such as analyzer sensitivity have impaired routine quantitative analysis by Auger electron spectroscopy. In the absence of accurate data concerning the factors in Eq. (10) most investigators have employed empirical calibration procedures. Weber and Johnson (35) deposited known amounts of potassium on a clean Ge(111) substrate and found that the peak-to-peak height of the K Auger transition in the second-derivative spectrum was a linear function of the fractional surface coverage in the submonolayer region. They derived a theoretical basis for this relationship based upon the assumptions that neither the peak shape nor peak position varied with the surface coverage. Sickafus (36) has summarized a number of calibration experiments which employed a quartz crystal oscillator microbalance, ellipsometry, interferometry, radiotracers and known coverage chemisorption as the bases for determining the absolute surface coverages. These studies generally found a linear

relationship between Auger signal intensity and coverage in the submonolayer region. Palmberg (37) has suggested that quantitative analysis could be accomplished through elemental sensitivity factors derived empirically from data on elemental standards, and he has shown that all elements can be assigned absolute sensitivity factors which are modified only by the backscattering factor which depends on the chemical environment. However, this method requires accurate data for the ionization cross sections, the escape depths and the backscattering factors; unfortunately, these data are not presently available. A further complication results from experimental difficulties in measuring the absolute Auger current since the peaks are superimposed on a large background which varies in magnitude and shape with the chemical environment.

LOW-ENERGY ELECTRON DIFFRACTION

Significant developments in the theory of low-energy electron diffraction (LEED) have occurred in the last few years. There is a widespread consensus that present theoretical models of LEED are quantitative in nature. The dream of surface structure determination via LEED which began with the classical experiment of Davisson and Germer (38) in 1927 has finally been realized. The diverse approaches proposed at the beginning of the development of LEED theory in the last decade are converging gradually into a few standardized methods of theoretical analysis. The modern mathematical models of electron solid scattering are apparently adequate for quantitative surface structure determination, but the systematic applications of modern theoretical analyses to interpret suitable comprehensive data are still in their infancy.

Introductory material concerning the theory and the practical application of LEED to the study of surfaces can be found in the previous work done in this laboratory by Summers (39). The configuration of the diffracted beams and their variations in intensity with incident electron energy and angle of incidence can be measured experimentally. The only information conveyed by the configuration of the beams is the translational symmetry parallel to the surface of the two-dimensional, geometrically-equivalent layers of atoms that comprise the solid.

Determination of the unit cell structure within each of these layers and of the packing sequence of the layers relative to each other requires analysis of the diffracted intensities. In order to perform intensity analysis, a rather complete theory relating the intensities to the microscopic parameters, e.g., atomic positions and thermal motions, which characterize the surface must be constructed and then appropriately simplified and reduced to computational algorithms suitable for analysis of measured intensities.

All presently employed LEED models are based upon the hypothesis that the adsorbate-substrate system forms an atomically flat, planar, single domain crystal surface. Within the confines of the planar surface hypothesis two fundamentally different approaches have been proposed to determine the atomic geometries of surfaces. The objective of microscopic model approaches is the development of a model of electron solid scattering which describes measured LEED intensities from solid surfaces. This approach requires a model for the electron-ion-core potential which causes the large angle scattering of the incident electrons, an expression for an optical potential to simulate the consequences of electron-electron interactions on elastic electron-solid scattering, i.e., the real part of the optical potential causes refraction of electrons at the vacuum interface and the imaginary part describes the removal of electrons from the elastic beam by inelastic electron-electron collisions,

and a Debye-Waller factor to describe the reduction of the elastic particle-ion-core scattering amplitudes by the thermal motion of the ion cores. Extensive sensitivity analyses (40) have established three major conclusions about these parameters: (1) simple overlapping-atomic-potential models seem adequate for the purpose of surface structure determination to within $\Delta d \approx 0.1$ Å, (2) crude empirical models of the electron-solid optical potential appear to be sufficient and (3) low temperature ($T \leq 100$ K) intensity data should be used in order to separate vibrational and geometrical effects. The mathematical formulations of the various models currently in use for intensity analysis are discussed in more detail in the recent literature (41-43).

The data reduction approach is based on the fact that despite the occurrence of strong dynamical (multiple-scattering) phenomena, both model calculations and LEED intensity data exhibit unmistakable residual manifestations of the purely geometrical conditions for intensity maxima which characterize kinematical (single-scattering) analyses. By manipulating observed LEED intensities to enhance these geometrical effects while smoothing or ignoring the dynamical ones, analytical procedures based on kinematical concepts can be used for structure determination. The kinematic formulation and its extensions and the insights derived from that formulation have been reviewed by Webb and Lagally (44).

Questions concerning the uniqueness of the conclusions drawn from model calculations as well as their intrinsic precision arose when different analyses of LEED intensities from Ni(100)-C(2x2)-S and Ni(100)-C(2x2)-O surfaces did not lead to identical structures. Demuth, Jepsen and Marcus (45) examined these structures and found that both sulphur and oxygen sat in four-fold holes at distances of 1.30±0.1 and 0.90±0.1 Å above the plane passing through the center of the underlying nickel layer; however, Duke et al. (46) calculated a distance of 1.70±0.1 Å for the sulphur structure; and Andersson et al. (47) found the best fit for an oxygen distance of 1.50±0.1 Å. These discrepancies prompted consideration of the possibility that more than one atomic geometry may be associated with a given surface translational symmetry. The reproducibility of the intensity data, the accuracy with which the properties of the spectrometer were known, the completeness of the characterization of the surface structure by independent measurements and the dependence of the uniqueness of a structure on the extensiveness of the data were also considered as possible sources of the disagreement. The causes of these particular discrepancies were eventually discovered. After the energy scale of the experimental data had been corrected by -2.5 eV in order to compensate for a contact potential difference between the electron gun and the collector, Duke and Lipari (48) found that a Ni-S distance of 1.30 Å provided a slightly better fit to their data. Pendry

(as cited in 49, 50) favored a Ni-O distance of 0.9 Å after he had extended his calculations to higher energies. The apparent equivalence of the various computation procedures was reinforced when Van Hove and Tong (49) calculated nearly identical distances for O, S, Se and Te (2x2) overlayers on Ni(100) as Marcus et al. (50) for the same experimental data. While the various computation schemes appear to be equally satisfactory, the problems associated with data reproducibility and limited data bases have been dramatically underlined. Duke, Lipari and Laramore (51) feel that an extensive array of low temperature data consisting of at least 50-70 maxima in 6-10 beams for several angles of incidence is necessary for an accurate intensity analysis.

REVIEW OF PREVIOUS RESEARCH ON THE INTERACTION OF NITRIC OXIDE WITH RUTHENIUM

The requirement that nitric oxide be virtually eliminated from automobile exhaust has generated considerable interest in the development of an inexpensive, plentiful and effective catalyst suitable for this task. After extensive studies (52, 53) of the rates of the heterogeneous decomposition of nitric oxide over a large variety of catalysts showed that this reaction was so slow that an excessive amount of catalyst would be necessary for the effective removal of the NO, emphasis was placed on chemical reduction processes which were known to be orders of magnitude faster than the decomposition reaction. Over a decade ago Sourirajan and Blumenthal (54) found that a 5-10 fold excess of either carbon monoxide or hydrogen or both would remove 90% of the NO from exhaust gases at 300° C over a CuO/SiO_2 catalyst. They proposed the use of a two-stage catalytic converter: the first bed would be operated in a chemically reducing atmosphere where excess CO would reduce NO, air would be added between the beds and the remaining CO and hydrocarbons would be oxidized over the second bed. However, they also discovered one drawback to the proposed scheme. Depending upon the experimental conditions, from 20 to 98% of the NO was reduced to NH_3. This ammonia would be subsequently reoxidized back to NO in the second bed of an actual converter system.

The production of large amounts of NH_3 was somewhat surprising since there is typically about four times as much CO as H_2 in automobile exhaust; and it was assumed that the major path to NO reduction would be:

$$NO + CO \rightarrow \tfrac{1}{2}N_2 + CO_2 \quad . \qquad (11)$$

This paradox was resolved when Jones et al. (55) found that their Pt catalyst was active for the water-gas shift reaction:

$$CO + H_2O \rightleftarrows H_2 + CO_2 \quad . \qquad (12)$$

The hydrogen formed by this reaction efficiently reduced NO to NH_3 on the same catalyst:

$$NO + \frac{5}{2}H_2 \rightarrow NH_3 + H_2O \quad . \qquad (13)$$

The water-gas shift equilibrium is an important factor in determining the composition of exhaust gas at fuel-rich stoichiometries. The equilibrium is frozen far to the left in the combustion and expansion processes in automobile engines, and equilibrium is not maintained as the gases cool. The equilibrium ratio of H_2 to CO increases dramatically at lower temperatures; as a result, if the catalyst can re-establish this equilibrium at the catalyst operating temperature, the dominant reducing species will be H_2 instead of CO (56). The water-gas shift reaction was established as the major source of hydrogen on the surface of the catalyst after it was found that the saturation coverage of hydrogen from adsorbed hydrocarbons under dry conditions was very small and that the steam

reforming surface reaction was slow compared to the water-gas shift reaction (57).

Shelef and co-workers (1, 58, 59) have conducted an extensive study of NH_3 formation during the reduction of NO by H_2. They have proposed a simple "nitrogen pairing" model to account for the variations in the N_2/NH_3 product ratio: in the formation of NH_3, only one NO molecule need participate in a possible rate-limiting event on the surface, whereas for NO defixation two NO molecules are necessary. If the rate of NH_3 formation is a linear function of surface NO concentration and the rate of unfixed products formation a quadratic function, a decrease in NO surface concentration will suppress defixation more than conversion to ammonia. The influences of CO and O_2 on the amount of NH_3 produced can be rationalized with this model. The observed increase in NH_3 production with increased CO concentration can be explained by postulating that CO and NO compete for the same surface sites, i.e., the presence of CO on the surface will block the adsorption of NO. Oxygen can decrease NH_3 production by converting CO to CO_2 which, if it then desorbs, would unblock the surface.

During the course of this study, it was observed that supported Ru catalysts had a higher selectivity for the formation of N_2, instead of NH_3, during NO reduction than most other commonly employed catalysts. An attempt was made to trace the path of the N atoms from NO molecules to

N_2 during the reduction of NO by H_2 on Ru/Al_2O_3 in order to determine whether ammonia was a gas-phase intermediate (59). They found no evidence for actual release of NH_3 into the gas phase. They concluded that it was possible that the intermediate product might not be the gaseous ammonia molecule but rather partially-hydrogenated fragments which pair up in the same manner as during the catalytic decomposition of NH_3. They surmised that the difference between Ru and most other catalysts is that the mechanism of nitrogen formation governing ammonia decomposition is only operative on Ru which has the unique ability to both decompose and synthesize ammonia.

Klimisch and Taylor (2) have also investigated NH_3 production during the reduction of NO by H_2 over Pt, Pd and Ru catalysts. They were able to correlate the N_2/NH_3 product ratio with the ability of a catalyst to promote the decomposition of NH_3. The Pt catalyst was moderately effective in removing NO, but considerable NH_3 was produced which corresponded to a rather poor ability of the catalyst to decompose NH_3. Ammonia formation was fairly small and relatively constant (~20%) for temperatures above 450° C over a supported Ru catalyst. They observed also that the activity of a Ru catalyst changed after it had been exposed to excess oxygen at elevated temperatures. This oxidized form of the catalyst produced only minimal amounts of NH_3 for temperatures above 500° C. The original activity could be regained by reduction of the

catalyst at 700° C. Even though the difference in NH_3 production between the two states of the catalyst correlated with the difference in ammonia decomposition activity, additional studies (3) indicated that an ammonia intermediate did not appear to be involved in NO reduction over reduced Ru/Al_2O_3 and was only a minor pathway to N_2 over the oxygen-treated catalyst. The low NH_3 yield over Ru was attributed to strong NO chemisorption since that would tend to increase the probability of adjacent N-species on the surface under all conditions. The results of Kobylinski and Taylor (5) supported these findings since they found that ammonia decomposition was not responsible for the high selectivity toward N_2 observed with Ru catalysts.

Klimisch and co-workers (3, 4, 6) have made an extensive investigation of the two activity states exhibited by supported Ru catalysts. Conversion of the catalyst between the two states was reversible and accomplished by oxidizing or reducing the catalyst. The unique selectivity of Ru for reduction of NO to N_2 did not change appreciably for the two states. They found that the oxygen-treated catalyst was active for the water-gas shift reaction, ammonia decomposition and hydrocarbon formation from CO and H_2, while the reduced catalyst was basically inert. They found that this "dual state" phenomenon also occurred for Pt and Pd catalysts as well. The catalytic activity of a supported Ru catalyst did not depend upon the formation of ruthenium dioxide or the degree of metal

dispersion. They suggested that the transformation to the more active oxidized catalyst state involved a reconstruction of the surface and/or destruction of inhibiting metal-support interactions.

The complexity of the catalytic behavior of metallic ruthenium was underscored by the recent study of Voorhoeve and Trimble (60). During their study of the reduction of NO by a mixture of CO, H_2, H_2O and CO_2, they found that there were five reproducible states of the catalyst with characteristic conversion patterns. There were states analogous to the two previously reported plus another reduced state formed by reduction with H_2 at 600° C which was active in the water-gas shift reaction and did not promote NH_3 formation above 500° C. The other activity states were formed by exposing a fresh catalyst to air and by treating a catalyst with SO_2. They suggested that nitrogen incorporation into the surface was responsible for the high NH_3 production and low NH_3 decomposition activity at temperatures above 500° C associated with the previously reported reduced state of the catalyst. Oxygen treatment was assumed to remove the nitrogen from the surface and replace it with some oxygen.

Modern surface measurement techniques have only recently been applied to the NO/Ru system in attempts to identify the chemisorbed species present on the surface during the reduction of NO. Ku, Gjostein and Bonzel (8) employed LEED, AES and thermal desorption spectroscopy to study the chemisorption of NO on a Ru(10$\bar{1}$0) single crystal sample.

The experimental evidence strongly favored an adsorption model in which NO dissociatively adsorbed into separate nitrogen and oxygen phases. Once the surface was saturated with the dissociated NO phase, further NO adsorption occurred into a molecular state. The nitrogen phase was unstable at temperatures as low as 200° C. The N_2-selectivity of Ru catalysts was attributed to the ability of Ru to dissociatively adsorb NO and to the short residence time of N adatoms at elevated temperatures which inhibited the formation of surface complexes with H_2 or CO which could eventually lead to NH_3 formation. This investigation was followed by an ultraviolet photoemission study (9) of NO adsorption on Ru(10$\bar{1}$0) and Pt(100). For NO on Pt a UPS spectrum characteristic of molecular NO was identified; and the spectrum for Ru clearly indicated dissociation of NO into atomic N and O. For high NO exposures the UPS spectrum showed evidence for molecular NO in addition to the dissociated species. The low temperature production of NH_3 over Ru and the copious production of NH_3 over Pt at all temperatures were attributed to the presence of molecular NO on the surface.

EXPERIMENTAL

Purpose of Experiments

Numerous kinetic studies have found that supported Ru catalysts exhibit high selectivity for the reduction of NO to N_2. This discovery is not surprising in view of the unique chemistry of Ru with nitrogen ligands (61). The strong Ru-NO bonding as well as the remarkable interactions of N_2 with Ru are consistent with the N_2 selectivity. While the characterization of the simpler NO/Ru gas-solid adsorption system by ultrahigh vacuum techniques has produced a reasonable explanation for the observed selectivity, i.e., the ability of Ru to adsorb NO dissociatively and the instability of N adatoms at moderate temperatures, these studies have shed no light upon the complex variations in catalytic activity with catalyst pretreatment.

A primary aim of the LEED/AES approach to catalysis is to find correlations between structure and catalytic activity, because the efficiency of a catalyst is related directly to the surface atomic arrangement. Monitoring the surface with LEED allows the existence of potentially important catalytic processes such as order-disorder transitions at critical temperatures, segregation of new phases and island growth to be established. Catalysis may proceed directly above a reconstructed sublayer which then acts as the actual catalyst rather than the undisturbed substrate. Previous work in this laboratory on

the NH_3/W system has demonstrated that the steady-state decomposition of NH_3 at elevated temperatures and pressures proceeded on ordered surface structures not previously detected under milder conditions (39). In order to determine the possible existence of similar catalytically active ordered surface phases for the NO/Ru system, NO was allowed to interact with Ru in a steady-state manner at reactant partial pressures $\leq 10^{-6}$ torr and temperatures $\leq 950°$C. The structures resulting from the interactions with oxygen were also determined.

These experiments were performed on a Ru(10$\bar{1}$0) single crystal sample. The (10$\bar{1}$0) plane (see Fig. 7c) was chosen for a variety of reasons. It is a fairly close packed face (8.6×10^{14} atoms/cm^2) and should have a low surface free energy and, thus, good thermal stability to rearrangement or disordering. This surface has a fairly open structure whose dominant feature is the troughs than run parallel to the [010] direction. These troughs should play a significant role in adsorption and surface diffusion processes. The (10$\bar{1}$0) plane of a hcp metal is very similar to the fcc (110) surface (they differ in coordination numbers of the surface and second-layer atoms), and there have been a large number of adsorption studies reported for these surfaces. A LEED/AES study of NO on Ru(10$\bar{1}$0) at low temperatures and pressures has been published (8) which provided a means of checking the characteristics of the experimental apparatus against those of other

investigators outside this laboratory.

Experimental Apparatus

The experimental studies were performed in a pyrex ultrahigh vacuum chamber which contained Physical Electronics 4-grid LEED optics and a quadrupole mass spectrometer. The system was pumped with an ion pump, and the base pressure after bakeout was $\sim 2 \times 10^{-10}$ torr. The apparatus has been described in detail elsewhere (39).

The single crystal Ru sample used in this study was cut from a zone refined single crystal supplied by MRC Corporation. It was orientated using Laue x ray techniques and cut to expose a $(10\bar{1}0)$ plane at its surface. The sample disc was mechanically polished to a mirror finish on both sides. The final thickness was ~ 1.5 mm; the total surface area was 1.1 cm^2. The sample was spot-welded to a 0.46 mm diameter tungsten wire which in turn was welded to the heavier support lead of a glass press seal. The support lead could be immersed in liquid nitrogen which enabled the sample to be cooled to -50° C. The sample could be heated by electron bombardment on its rear surface. Temperatures were measured using a W/Re5% - W/Re26% thermocouple (0° C reference junction) spot-welded to the back of the crystal.

The nitric oxide (99%) was obtained from Matheson. It was vacuum distilled in order to remove volatile contaminants and then transferred from a liquid-oxygen cooled cold finger into a breakseal ampule held at

liquid-nitrogen temperature in order to prevent the transfer of less volatile nitrogen oxides. Mass spectral analysis of the purified NO showed no detectable impurities. Oxygen and hydrogen were obtained from Ag and Pd-Ag25% leak diffusers.

Auger Spectrometer

The Auger electron spectrometer used in this study was a hybrid instrument. The Physical Electronics LEED controller was used to operate the electron gun, and the analyzer section of the optics (grid meshes and fluorescent screen) was controlled by a Vacuum Generators Auger Electron Detector. The only modification necessary to interface the LEED and Auger instrumentation was to disconnect the screen and the retarding grids from the LEED electronics and to connect them to the preamplifier and the programmable high-voltage power supply.

A schematic diagram of the circuit used to obtain the differential Auger spectrum in shown in Fig. 2. The potential on the retarding grids is supplied by a programmable high-voltage (0 - 2.5 keV) power supply. The programming voltage is a linear ramp supplied by an integrating circuit. A sinusoidal modulation from a low-distortion oscillator is superimposed on the retarding potential by a transformer. The oscillator is tuned to 4.75 kHz for the first-derivative spectrum and to 2.375 kHz for the second. In order to achieve a high input resistence and hence a good signal-to-noise ratio and also a low order of spurious

response to unwanted signals, the input transformer of the preamplifier is tuned to form a bandpass filter. The inductance of the transformer is in parallel with the distributed capacitance (~300 pf) of the collector circuit, and this LC tank selects that portion of the collected current that varies at the desired harmonic of the modulation signal. At resonance the impedance of the tank is purely resistive and is about 10^7 ohms.

The LEED electron gun is capable of producing a monoenergetic beam of electrons with kinetic energies up to 1.5 keV and currents of ~10 - 100 μa. A primary beam energy of 1.4 keV was normally used. The beam current should be as small as possible in order to minimize any destructive interactions between the incident electrons and the system under study, but it must be large enough to generate a detectable signal. A beam current of 50 μa proved to be about the minimum current that would produce an acceptable signal-to-noise ratio for submonolayer coverages of oxygen and nitrogen.

The increased sensitivity of the derivative spectrum over the total yield is purchased at the expense of bandwidth. The bandwidth, which is essentially the reciprocal of the measurement time constant, is limited by the statistical noise associated with the measurement of discrete charges, i.e., shot noise. Since shot noise is proportional to the bandwidth (62), the signal-to-noise ratio can be improved by decreasing

the bandwidth, i.e., increasing the measurement time. The spectrometer was normally operated with a bandwidth of 0.1 Hz which limited the rate at which the spectrum could be generated to the order of 1 eV/s.

The sensitivity of a surface analytical technique is stated properly in terms of the smallest fraction of a monolayer on which a meaningful measurement can be made. It is limited by the background against which the signal appears. If the peak-to-peak height in the second-derivative spectrum is assumed to be a linear function of the surface coverage, then the sensitivity of an Auger spectrometer can be estimated by comparing the average background level to the peak height for a known adsorbate coverage. If a signal-to-noise ratio of two is arbitrarily chosen as the limit of detectability, the estimated sensitivity of this instrument under normal operating conditions is 0.04 monolayers of oxygen or nitrogen adatoms.

If a monoenergetic beam of electrons of energy E is injected into the spectrometer, a peak of full width at half-height, ΔE, is recorded in the spectrum due to various instrumental limitations. The ratio $E/\Delta E$ defines the resolution, while its reciprocal expressed as a percentage is referred to as the instrumental linewidth (ILW). Limitations on the resolution may be divided into two groups, those that are proportional to electron energy ($\Delta E/E$ = const) and those that are independent of electron

energy (ΔE = const). The former group includes: (1) potential variations across the space between the wires of the meshes, (2) deviations of the grids from ideal spherical geometry and (3) effects of finite beam size and improper positioning of the sample. The latter group consists of: (1) the energy spread of the primary electrons, (2) stray magnetic fields and (3) the ac modulation voltage on the retarding grids.

The resolution of this instrument at various values of electron energy was determined by recording the elastic peak in the N(E) spectrum

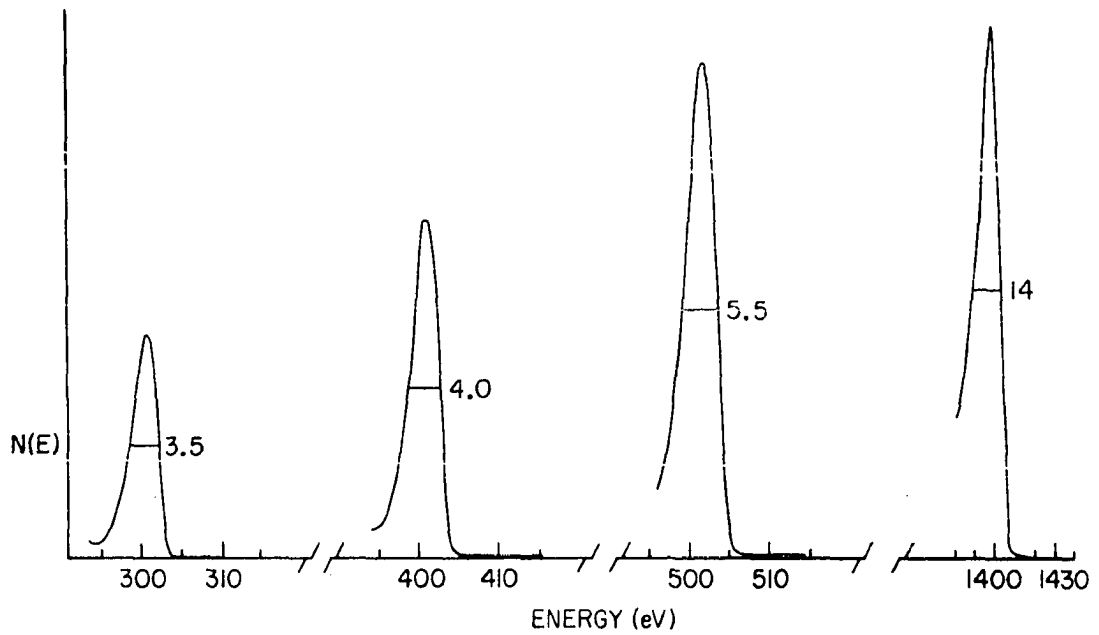

Fig. 4. Experimental determination of the instrumental linewidth ($\Delta E/E$ x 100%). The full width at half-height of the elastic peak in the N(E) spectrum (ΔE) was measured at various primary beam energies (E).

(obtained by tuning the spectrometer to the fundamental component of the modulation frequency) and then measuring the full width at half-height (see Fig. 4). The observed ILW is approximately 1% for electron energies between 300 and 1400 eV. The incident beam is very nearly monoenergetic since the energy spread is on the order of 3/2 kT or about ±0.3 eV for a tungsten filament at 2200° C. The spectrum was taken with an ac modulation amplitude of 0.4 volts; and since, according to Park and Houston (29), the N(E) spectrum is smoothed by an instrument response function of the form:

$$T(E, k) = \frac{2}{\pi}\left[1 - (E/k)^2\right]^{\frac{1}{2}} . \qquad (14)$$

The full width at half-height due to the potential modulation should be $\sqrt{3}k$ or only about 0.7 eV. The observed ILW is due mainly to field penetration in the grids.

RESULTS

The Clean Surface

Auger spectra taken before the sample was cleaned showed the presence of large amounts of carbon, sulphur and oxygen. The overlap of the carbon Auger peak with the very intense Ru_{278} peak made the identification of surface carbon very difficult. The following scheme was used to analyze the data for carbon: the peak at 278 eV was considered to be composed of both Ru and carbon; as a result, the ratio of this compound peak to a peak due solely to Ru has a minimum value when there is no carbon on the surface. Outgassing the sample at 1300° C for several days was sufficient to remove the sulphur and most of the carbon and oxygen; but it did not produce a clean LEED pattern. The LEED spots were streaked and diffuse, and there was a high background level. A very complex, incomplete LEED pattern usually formed upon cooling.

A clean surface was finally obtained after repeated cycles of heating the crystal to 1200° C followed by argon bombardment and finally annealing below 1000° C. When the pressure in the vacuum chamber was increased to 1×10^{-3} torr with argon, the polarity on the LEED gun anodes reversed and the sample biased several hundred volts below ground, the LEED gun was capable of producing a beam of Ar^{+} ions

($\sim 5\ \mu a/cm^2$, 800 eV). The LEED pattern for the annealed surface had sharp spots on a dark background. The Auger spectrum of the clean surface shown in Fig. 5 was identical to those of Grant and Haas (7) and

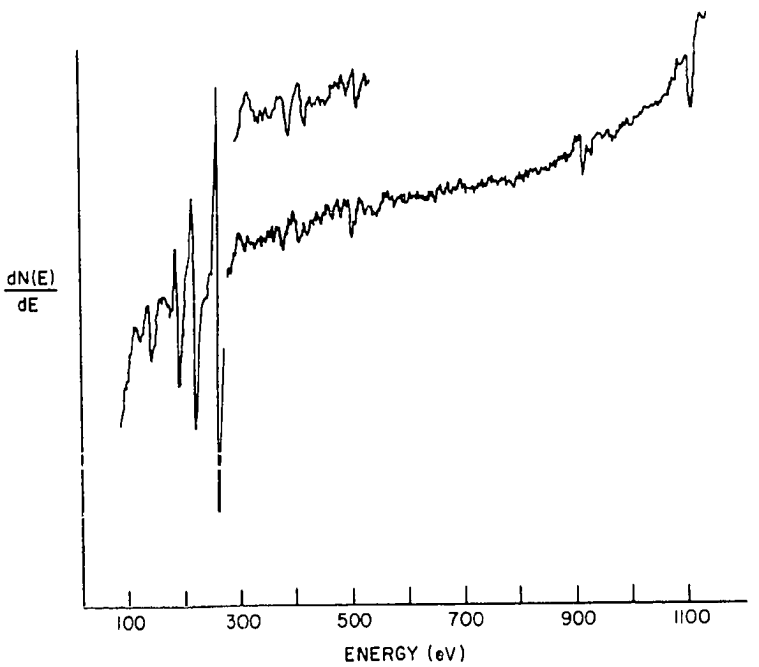

Fig. 5. Second-derivative Auger spectrum of a clean Ru(10$\bar{1}$0) sample at 500° C. The insert is a partial spectrum of the same sample at 200° C. Primary beam energy = 1.4 keV; beam current = 50 μa; sweep rate = 1.5 eV/s; ac modulation voltage = 2 v (for electron energies below 300 eV) and 4 v (for energies above 300 eV); full scale deflection = 1×10^{-10} amperes.

Madey et al. (10) for Ru(0001) samples in the Auger electron energy range < 300 eV. In the electron energy range from 300 to 500 eV, several small peaks (~2 to 3% of the intensity of the Ru_{278} peak) were present. Similar "fine structure" was also observed in the two studies of Ru(0001) samples; but those peaks do not coincide in energy with those shown in the insert in Fig. 5. There were also features in the spectrum near 950 and 1120 eV.

The dependence of the positions of the features with energies greater than 300 eV on the primary beam energy was examined. It was found that the peaks between 300 and 500 eV were independent of E_o, while the positions of the peaks observed at 950 and 1120 eV (for E_o = 1.4 keV) were linear functions of the primary beam energy. The peak observed at 1120 eV had an extrapolated threshold energy of ~280 eV which corresponds to the M_5 core level binding energy of 279.9±0.2 eV found by Fuggle et al. (11) from their XPS measurements. This feature is a core level ionization edge. An incident electron can transfer part of its energy to a core electron; as a result, the core electron will be ejected with a kinetic energy (with respect to the Fermi level of the sample) of:

$$E_K = E_o - E_B - \epsilon \quad , \qquad (15)$$

where E_B is the binding energy of the core electron and ϵ is the energy of the scattered incident electron. The maximum kinetic energy of the ejected electron corresponds to $\epsilon = 0$. An ionization edge is generally

much weaker than an Auger peak since the ejected electron energies are distributed over all values less than the maximum.

The energy of the feature originally observed at 950 eV was equal to 65% of E_o and had a threshold energy of zero. It was eventually discovered that this anomalous peak was caused by the interaction of the incident beam with the anodes of the electron gun. The position of this feature on the energy scale was found to be equal to the potential applied to the focusing anode implying that these electrons are the elastically backscattered component of a second incident beam of kinetic energy $E_o' = e|V_{focus}|$. The effects of this second incident beam should be negligible since its intensity is only about 10^{-6} times the intensity of the true incident beam and since its elastic peak occurs outside the energy range of interest.

Examination of Fig. 5 will show that the small peaks in the Auger electron energy range 300 to 500 eV have temperature dependent peak heights. This temperature effect was reversible and without noticeable hysteresis. Similar features have been observed for Cu and Co (63), Ni (64) and Ru(0001) (10). All of these investigators have attributed these peaks to the diffraction of the emitted secondary electrons. If a diffraction process results in a greater mean-free-path for electrons of certain energies and directions of momentum in the crystal, inelastically backscattered electrons of these energies and directions can escape

from a greater depth in the solid, thus accounting for an excess number at these energies. This is an elastic scattering process, and in the same manner that the relative positions of LEED beams from different crystallographic planes are scaled by the lattice parameters, the relative energies of these features should be scaled by the ratio of the reciprocals of the squares of the lattice constants. As a result it seems reasonable that the energies of the diffraction peaks observed for Ru(10$\bar{1}$0) would not coincide necessarily with those found for Ru(0001) samples.

Since this is a diffraction process, it will be dictated by the long range order of the crystal which is reduced (as far as the electrons are concerned in the adiabatic approximation) when the crystal is heated; therefore, the temperature dependence of these features should be characterized by a Debye-Waller factor. Laramore (65) has shown by assuming a spherically symmetric mode of vibration for the surface atoms and by using the harmonic approximation, the kinematic approximation for diffraction and the high temperature limit of the Debye model of lattice vibrations that the logarithm of the intensity, I, of a diffraction peak varies approximately with substrate temperature, T, according to:

$$\frac{d\,\ell n\, I}{d\,T} = -\frac{12h^2\cos^2\phi}{mk_B\lambda^2\theta_D^2} \qquad (16)$$

where ϕ is the angle between the direction of the incident beam and the direction of the diffracted backscatttered electron, λ is the wavelength of the electron and θ_D is the effective Debye temperature.

According to Duke and Laramore (66) the effective Debye temperature will be a function of the amplitudes of vibration of the surface and bulk atoms, the electron wavelength and the relative scattering power of surface and bulk atoms. The usual interpretation of the energy dependence of θ_D is that the surface atoms vibrate with larger mean square amplitudes than bulk atoms and that the energy dependence arises from the energy dependence of the electron elastic mean free path. The effective Debye temperature is less than the bulk value at low electron energies and approaches the bulk value at higher energies.

Plots of $\ln (I/I_o)$ of the peaks at 390 and 417 eV versus temperature are shown in Fig. 6. The quantity I_o is the intensity of the diffraction peak extrapolated to T = 0 K. Assuming that $\phi = 0°$ the slopes of these lines yield effective Debye temperatures of 324 and 330 K. These values are in good qualitative agreement with the values found by Madey et al. (10) from an analysis of the temperature dependence of LEED intensities from Ru(0001) and with the bulk Debye temperature of 400-426 K. The intensities of these features reached limiting values above 600° C. Since the theoretical interpretation predicts that the intensities should continue to decrease as the temperature is increased, it was assumed that the

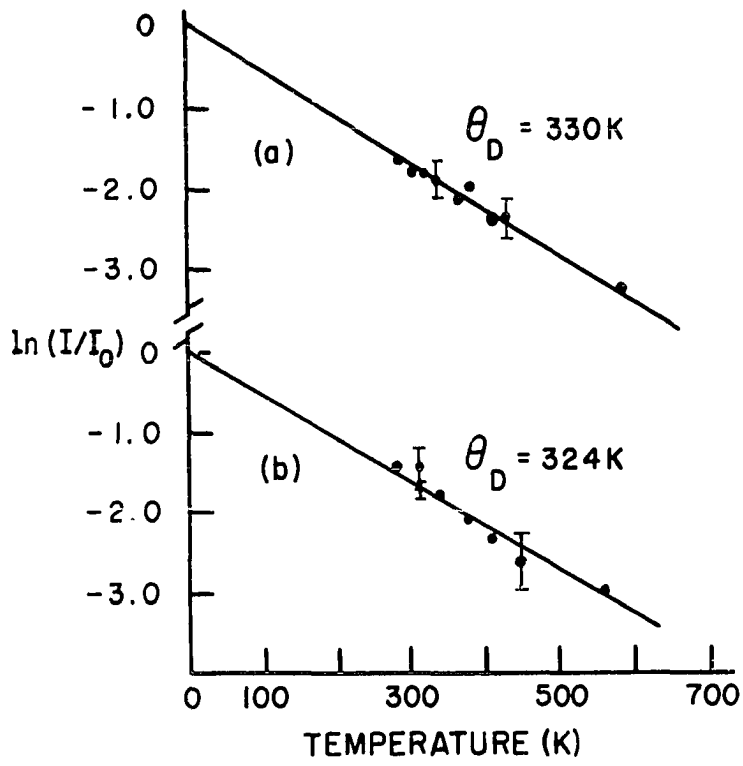

Fig. 6. Temperature dependence of the intensities of the diffraction features at (a) 417 and (b) 390 eV (I_o is the intensity at T = 0 K).

limiting intensities were due to the presence of a small amount of titanium on the surface; and these values were substracted from the intensities at lower temperatures. This assumption is based on the following facts: (1) the major Ti Auger peaks occur at 380±5 and 417±7 eV, (2) spark-source mass spectral analysis of the Ru rod from which the sample was cut showed the presence of 200 ppma of Ti and (3) some intensity is observed at these energies even after Ar^+ bombardment. Madey et al. (10) surmised that the peaks near 400 and 420 eV in their Auger spectra could conceivably be due to impurity Ti. Fuggle et al. (11)

did not find any XPS peak ascribable to Ti, but they stated that an amount of less than 5% of Ti would have remained undetected because of neighboring Ru peaks. Measurement of the true peak heights from the spectra is very difficult since these peaks are very small. The observed peak heights ranged from 15 down to 2 arbitrary units (on the same scale, Ru_{235} would have a peak height of about 500 units), and the error bars represent an uncertainty of ±1 unit.

LEED Pattern from Clean Ru(10$\bar{1}$0) Surface

The LEED pattern from the clean Ru(10$\bar{1}$0) surface at a primary beam energy of 38 eV is shown in Fig. 7a. The electron beam is approximately 6° off normal incidence. The sample was not positioned at the center of the hemispherical optics; as a result, the LEED beams near the edges of the screen diverged distorting the pattern from the true rectangular symmetry of an hcp (10$\bar{1}$0) plane. The specular beam is masked by visible light from the hot tungsten filament which is reflected off the sample onto the phosphor screen. This light appears as a bright area in the middle of the left side of the photograph. The other bright region is the incandescent filament of the LEED electron gun. Figures 7b and 7c show the indexing of the diffraction pattern and the surface unit cell.

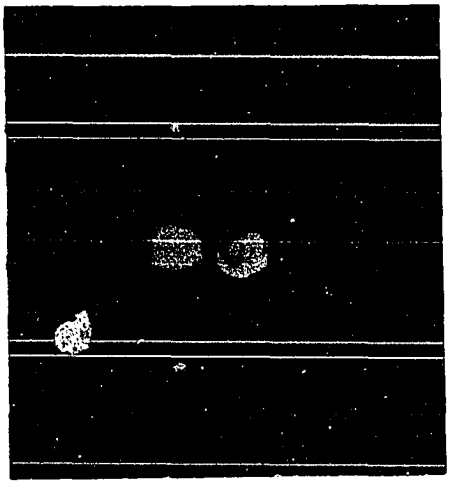

(a)

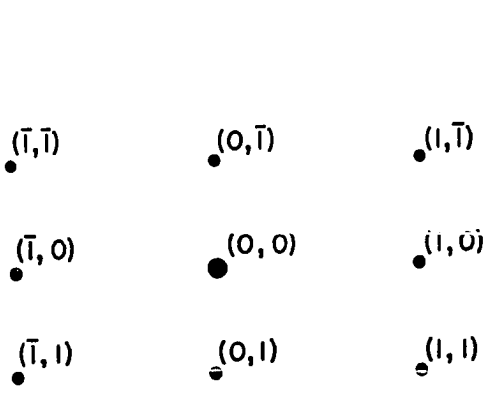

(b)

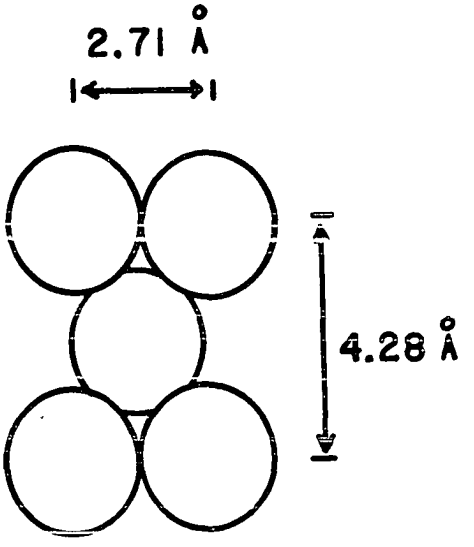

(c)

Fig. 7. LEED pattern, indexing and surface unit cell for Ru(10$\bar{1}$0): a) LEED pattern from the clean surface at 38 eV beam energy, b) indexing of beams and c) surface unit cell.

Auger Analysis of Adsorbed Gases

The Auger analysis of the chemical composition of the surface was based on the Ru_{235}, N_{388} and O_{517} peak-to-peak heights in the second derivative spectrum. The initial, clean Ru surface was a convenient internal standard so that the amounts of nitrogen and oxygen adsorbed were represented by the ratios of the peak heights, N_{388}/Ru°_{235} and O_{517}/Ru°_{235}, where Ru°_{235} was the peak height of the Ru transition at 235 eV before any gases were admitted into the vacuum chamber. The use of an internal standard avoids the difficulty of absolute calibration which is important in this case since it is very difficult to reproducibly set the beam current and modulation voltage. In order to compare results from different runs, all data were scaled to an arbitrarily chosen standard Ru°_{235} peak height. The temperature-dependent diffraction feature near 390 eV was superimposed on the N_{388} peak. This contribution to the intensity was estimated by measuring the height of the diffraction feature at 417 eV and multiplying this value by the ratio of these peaks for a clean surface.

According to Brundle (33) the substrate signal intensity in the presence of an adsorbate can be expressed as:

$$I/I_o = \exp(-\ell/\lambda\cos\phi) \quad , \qquad (17)$$

where I is the intensity for an adsorbate covered surface, I_o is the intensity for a clean surface, λ is the emitted electron escape depth and

ϕ is the angle of emission with respect to the surface normal. This expression is based upon the assumptions that the adsorbate forms a uniform layer, there is no contribution from backscattered electrons and the attentuation is of an exponential form; therefore, values of λ computed from this expression will likely be upper limits. Since ℓ can be expressed as θ times the diameter of the adsorbate and θ is proportional to the oxygen peak height, the value of I_o, the intensity at zero coverage, can be found from the intercept of a plot of ℓn I versus O peak height. Figure 8 is a plot of $\ell n\ (I/I_o)$ of the Ru_{235} Auger peak versus

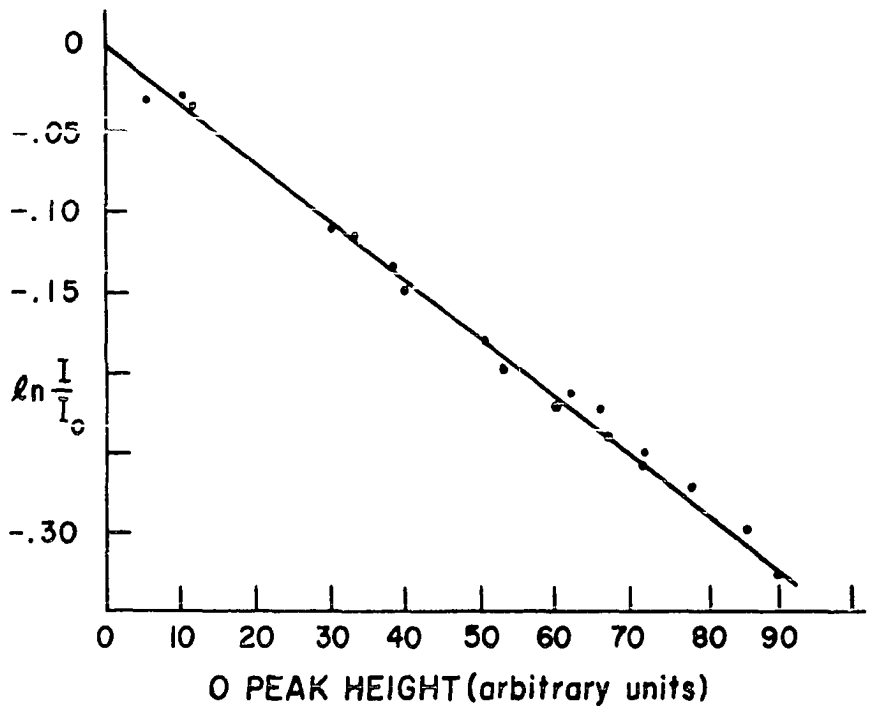

Fig. 8. Exponential attenuation of the normalized Ru(235 eV) Auger peak intensity (peak-to-peak height) as a function of the O(517 eV) peak height (I_o is the Ru intensity at zero coverage).

O peak height from four sets of data. This plot was used to determine I_o, i.e., Ru°_{235}, from measurements of I and O. The relative intensities for equal amounts of oxygen and nitrogen can be estimated from Eq. (10). Using literature values for σ, assuming $\lambda \propto E^{\frac{1}{2}}$ and including the instrumental resolution showed that the intensities should be nearly equal; therefore, when both oxygen and nitrogen were present on the surface, the abscissa in Fig. 8 was set equal to the sum of the N and O peak heights.

The data in Fig. 8 are replotted in Fig. 9 as I/I_o versus O/I_o. The

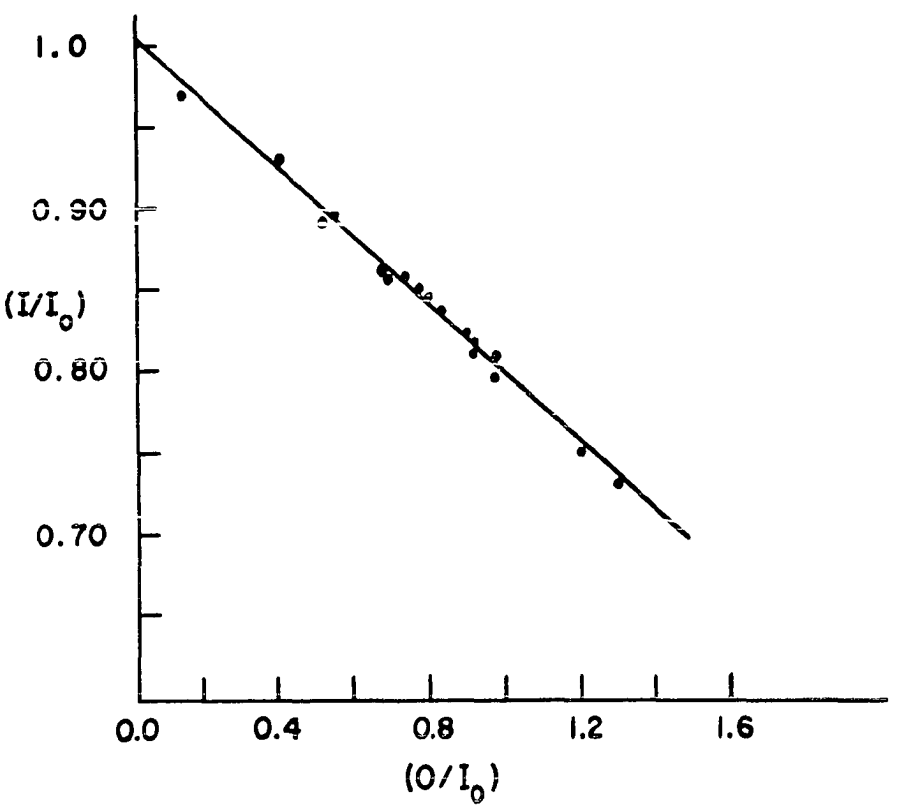

Fig. 9. Attenuation of the normalized Ru(235 eV) Auger peak intensity (peak-to-peak height) as a function of the normalized O(517 eV) peak intensity (I_o is the Ru intensity at zero coverage).

equation of the line is:

$$\frac{I}{I_o} = 1.004 - 0.215\left(\frac{O}{I_o}\right) \quad . \tag{18}$$

In the case of the dissociative adsorption of oxygen, ℓ is equal to 2.8θ (the adsorbed species is assumed to be O^{2-} with a diameter of 2.8 Å). The correlation among Auger results, observed LEED patterns and predicted overlayer structures, which will be discussed in detail in subsequent sections, shows that θ can be expressed as $0.625(O/I_o)$; as a result, $\ell = 1.75(O/I_o)$. Substituting for ℓ in Eq. (17), expanding the exponential and setting $\phi = 0°$ yields:

$$\frac{I}{I_o} = 1.0 - 1.75\left(\frac{O}{I_o \lambda}\right) + \cdots \quad . \tag{19}$$

It follows from Eqs. (18) and (19) that λ equals 8.1 Å to first order.

Instead of assuming that $\phi = 0°$ in Eq. (17), the angular dependence can be taken into account by considering the emission from a flat plate in the absence of an adsorbate. Assuming that the emission follows a cosine law, the emission in the presence of a film of thickness ℓ can be shown to be given by:

$$I = I_o\left\{e^{-x} - xe^{-x} + x^2\int_x^\infty x^{-1}e^{-x}dx\right\} \tag{20}$$

where $x = \ell/\lambda$. The integral on the right is a tabulated function. This equation can be solved by iteration to give $\lambda = 11.0$ Å. The calculated values are in good agreement with the escape depth versus electron

energy curve in the review article by Tracy and Burkstrand (67) which has $\lambda \sim 8$ Å for an electron energy of 235 eV.

LEED and Auger Electron Spectroscopy Results

The adsorption of NO on Ru(10$\bar{1}$0) at 90 and 200° C was followed by continually recording the Ru_{235}, N_{388} and O_{517} Auger signals. Since NO will decompose on hot filaments, the ion gauge was turned off during these experiments, and the gas-phase NO partial pressure was monitored with the mass spectrometer. The sample was dosed at a constant m/e = 30 ion current of 1×10^{-8} amperes ($\approx 2 \times 10^{-9}$ torr). The Auger beam input sufficient power (0.07 watt) and the thermal conduction of the crystal support lead was sufficiently small that the sample was held at a steady-state temperature of 160° C. Temperatures from 160 up to 750° C could be obtained by focusing a 1000 watt projector bulb on the back of the crystal, while placing liquid nitrogen in the sample support dewar assembly resulted in a minimum attainable temperature of -50° C. The adatom Auger peak heights as functions of dose time (exposure) are shown in Fig. 10. The ordinate of this plot is given in units of θ, the fractional surface coverage. Justification for this particular choice of a proportionality constant between peak height and θ will be presented later. The nitrogen portions of these fractional surface coverage versus exposure curves are in excellent agreement with the results of Ku et al. (8) (hereafter: KGB); the ratio of the nitrogen coverages at 200 and 90° C

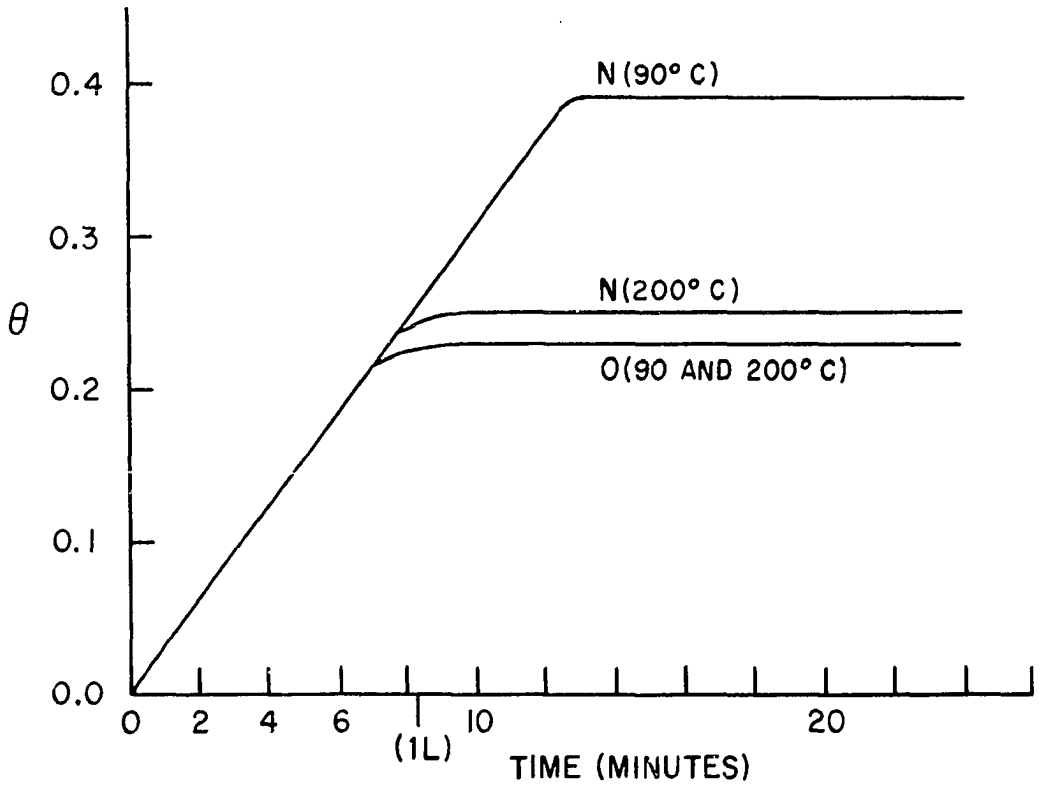

Fig. 10. Nitrogen and oxygen fractional surface coverages as functions of nitric oxide exposure ($P_{NO} \approx 2 \times 10^{-9}$ torr).

is within 2% of the reported value. No oxygen data as functions of exposure have previously been reported. The initial slope of these curves yields a sticking coefficient of 0.55 for nitric oxide.

According to the model proposed by KGB, the limiting N and O signals at 200° C represent the saturation coverage of chemisorbed atoms, and the increase in these signals at 90° C is due to the adsorption of NO into a molecular state. The lack of any increase in the O intensity at 90° C can be rationalized by postulating that the oxygen in this molecular state is so unstable that it is rapidly desorbed under the influence of the Auger

beam. A possible cause of this oxygen instability can be found in the results of an ultraviolet photoelectron spectroscopic study (9) of the adsorption of NO on Ru(10$\bar{1}$0). It was proposed that molecular nitric oxide adsorbed preferentially on adsorbed N atoms forming a molecular structure similar to N_2O which has the linear structure N-N-O. It seems reasonable that interaction of the exposed oxygen atoms with the incident electrons could result in their desorption as O^+ ions. The existence of these ions in the gas phase could not be verified since line-of-sight did not exist between the sample and the mass spectrometer. Some justification for the supposed weakness of the N-O bond can be found in the chemistry of Ru(II) ammine complexes. A $\left[Ru(NH_3)_5N_2O\right]^{2+}$ complex can be formed, but it is readily reduced by Cr^{2+} to the N_2 complex indicating that coordination of N_2O lowers the N-O bond strength (68).

Similar behavior has been observed by Usami and Nakagima (69) during their LEED/AES study of NO on W(100). The N and O peak heights increased at approximately the same rate until a monolayer had formed, and then the O peak began to decrease slightly while the N peak continued to grow until it was nearly three times as large as the O peak. This behavior was attributed to the electron-stimulated desorption of oxygen from a phase formed on top of the monolayer. Conrad, Ertl, Kuppers and Latta (70) stated that there was strong evidence for changes in the

adsorbate layer caused by the electron beam during their AES study of NO on Ni(111); however, they did not indicate the nature of the evidence.

This interaction between the O adatoms and the Auger beam can be parameterized in terms of a cross section, σ, for electron stimulated desorption. The rate of desorption can be expressed as (71):

$$\frac{dn}{dt} = -n\sigma\Phi \quad , \qquad (21)$$

where n is the adatom density, Φ is the incident electron flux and σ is the total cross section. In order for there to be no net increase in the oxygen signal as the molecular NO state becomes populated, the rate of oxygen desorption must be equal to the rate of adsorption. For an assumed beam diameter of 1 mm^2 and a cross section that is not a function of the adatom density, Eq. 21 gives a total cross section of 6×10^{-20} cm^2. This value is comparable to the 1.5×10^{-20} cm^2 for O_2 on W(110) found by Musket (71) and the $\sim 5 \times 10^{-20}$ cm^2 measured by Madey (72) for β_2-O on W(100). Additional support for the existence of a mechanism of Auger-beam-induced desorption of oxygen adatoms is found in the observation that, if the sample was dosed for twenty minutes with the beam off, the N and O signals were approximately equal. Oxygen desorption due to localized heating effects does not seem very likely since studies using field emission microscopy (73) and thermal desorption spectroscopy (8, 10) have shown that the onset of the thermal

desorption of oxygen from Ru occurs above 900° C.

When the LEED pattern is observed at 200° C under the same experimental conditions, the sequence of ordered surface structures shown in Fig. 11 as seen as a function of exposure, namely:

$$(1x1) \rightarrow C(2x4) \rightarrow (2x1) \quad .$$

LEED observations at 90° C indicate that with continued NO exposure, there is an increase in the background level and diffuse diffraction features begin to form near the $(h, k \pm \frac{1}{2})$ positions. These features have been attributed to the presence of molecular NO on the surface.

The adsorption of oxygen at a partial pressure of 2×10^{-9} torr at 200° C was followed by continually monitoring the O Auger signal. The fractional surface coverage of O adatoms as a function of exposure is shown in Fig. 12. The coverage increased linearly until $\theta = 0.2$ at which point the rate of adsorption began to decrease until it was nearly zero at $\theta = 0.3$. In order to determine whether the Auger beam had any influence upon the observed coverage, the gas-phase O_2 was pumped away after one experimental run. The O signal decayed with a cross section for electron-stimulated desorption of 1.5×10^{-20} cm^2. This beam-induced effect was confirmed by dosing for fifteen minutes with the beam off. The observed coverage was nearly 20% larger than for runs with the beam on continuously. Unfortunately, the beam-induced rate of desorption is of the same order of magnitude as the rate of

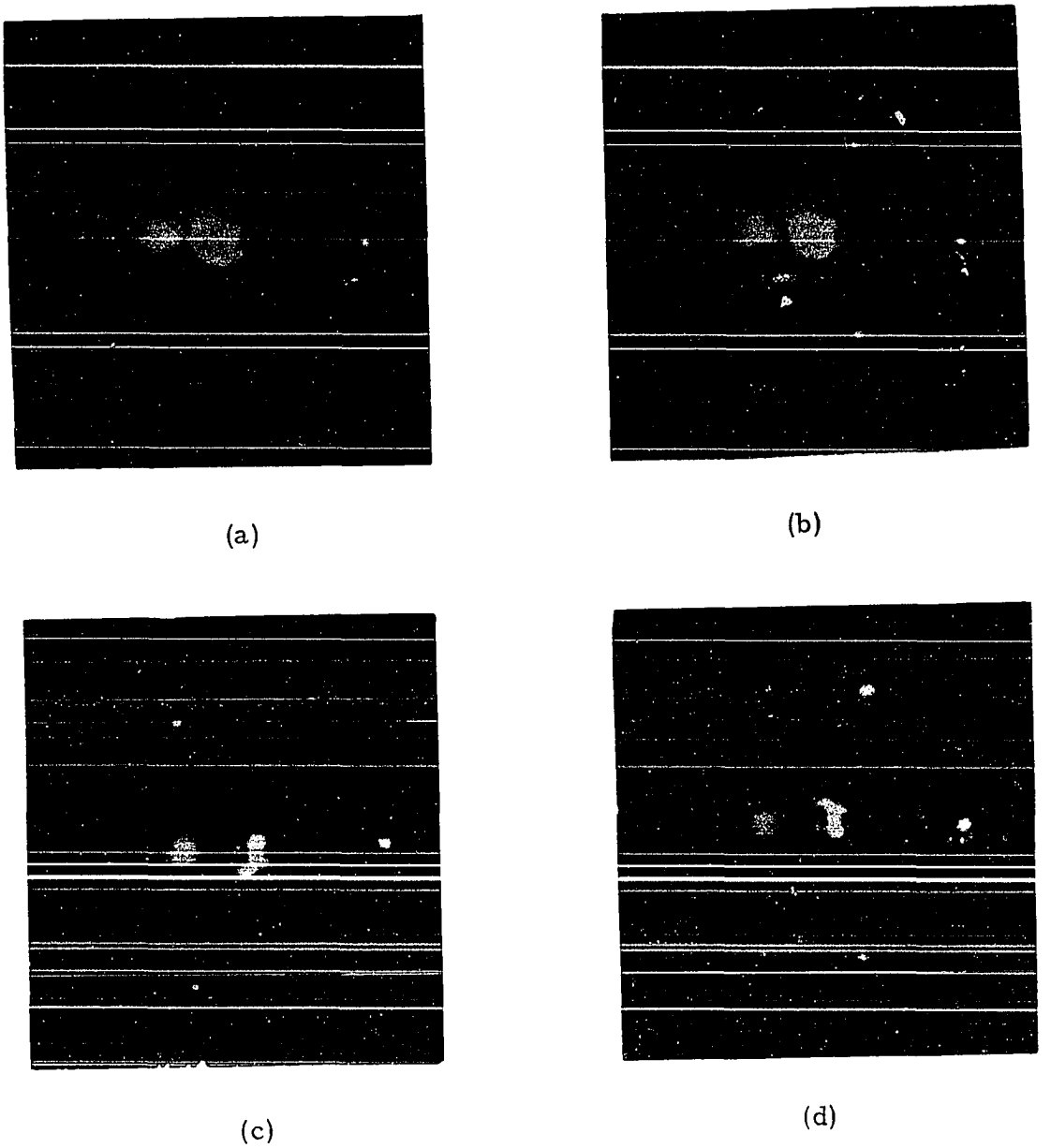

Fig. 11. LEED patterns resulting from the adsorption of NO or O_2 on Ru(10$\bar{1}$0) at T ≤ 200° C, 28 eV beam energy, a) (1x1) from clean surface, b) C(2x4), c) transition state: (h, k$\pm\frac{1}{2}$) spots have faded and (h$\pm\frac{1}{2}$, k$\pm\frac{1}{4}$) spots have merged, d) (2x1).

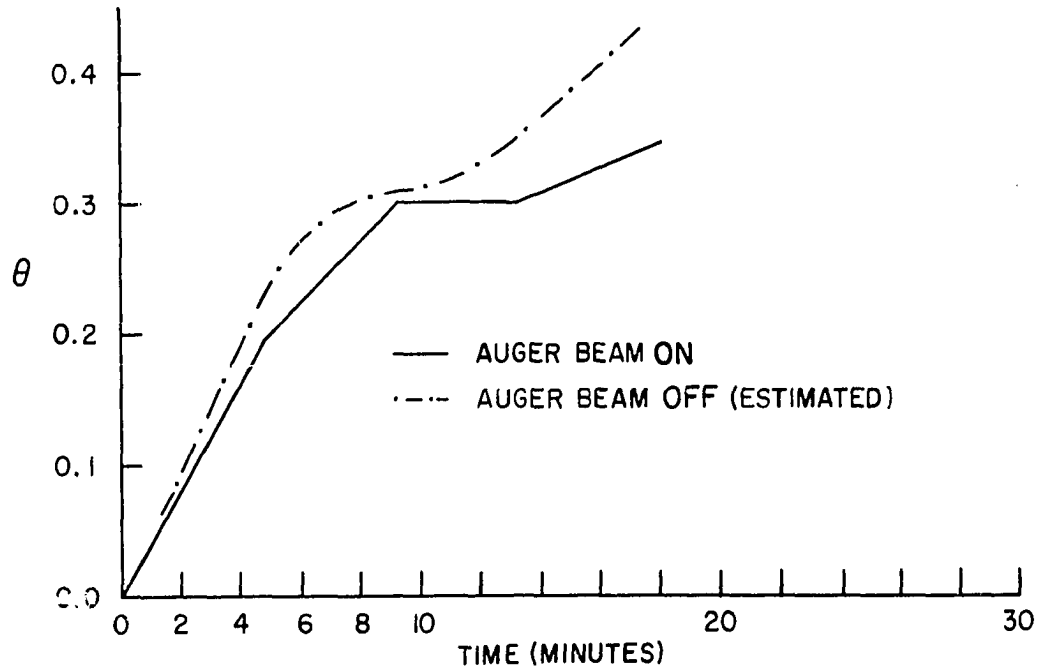

Fig. 12. Oxygen fractional surface coverage as a function of oxygen exposure ($P_{O_2} \approx 2 \times 10^{-9}$ torr) at 200° C.

oxygen adsorption at low dose pressures. The dashed curve in Fig. 12 is an estimation of the true adsorption behavior. The estimated initial sticking coefficient is 0.5 which is approximately equal to the initial sticking coefficient for NO adsorption at the same pressure. The saturation coverage was independent of temperature below 200° C and was approximately equal to the sum of the nitrogen and oxygen surface coverages from the adsorption of nitric oxide.

The adsorption of oxygen produced the same series of LEED patterns as the adsorption of NO. The region between six and ten minutes in

Fig. 12 where the surface coverage increased very slowly corresponded to the completion and subsequent fading of a C(2x4) LEED pattern. The rate of adsorption began to increase at the point where the $\frac{1}{4}$ order reflections had merged. There was no indication of the adsorption of oxygen into a molecular state at lower temperatures.

After long exposures to either NO or O_2, e.g., thirty minutes at 1×10^{-8} torr, at temperatures above 400°C, a C(2x6) LEED pattern was observed together with the (2x1). This compound pattern is shown in Fig. 13c. The relative intensities of the two patterns covered the entire range from sharp (2x1) and very faint C(2x6) at low temperatures to intense C(2x6) and faint (2x1) at elevated temperatures. Auger analysis of these compound surfaces showed fractional surface coverages of oxygen adatoms in the range 0.5 to 0.8. There was no indication of the presence of nitrogen on these surfaces within the limits of detectability (~0.04 monolayers of nitrogen adatoms).

The interaction between the Auger beam and the oxygen adlayer was described by a structure-sensitive cross section for electron-stimulated desorption. The cross section was 6×10^{-20} cm^2 for surfaces with $\theta > 0.6$, and it was approximately a factor of four smaller for surfaces with lesser coverages. A similar decrease in the surface coverage could be effected by pumping on the surface. If, after a compound surface had been formed, the system was then evacuated, the coverage decreased to

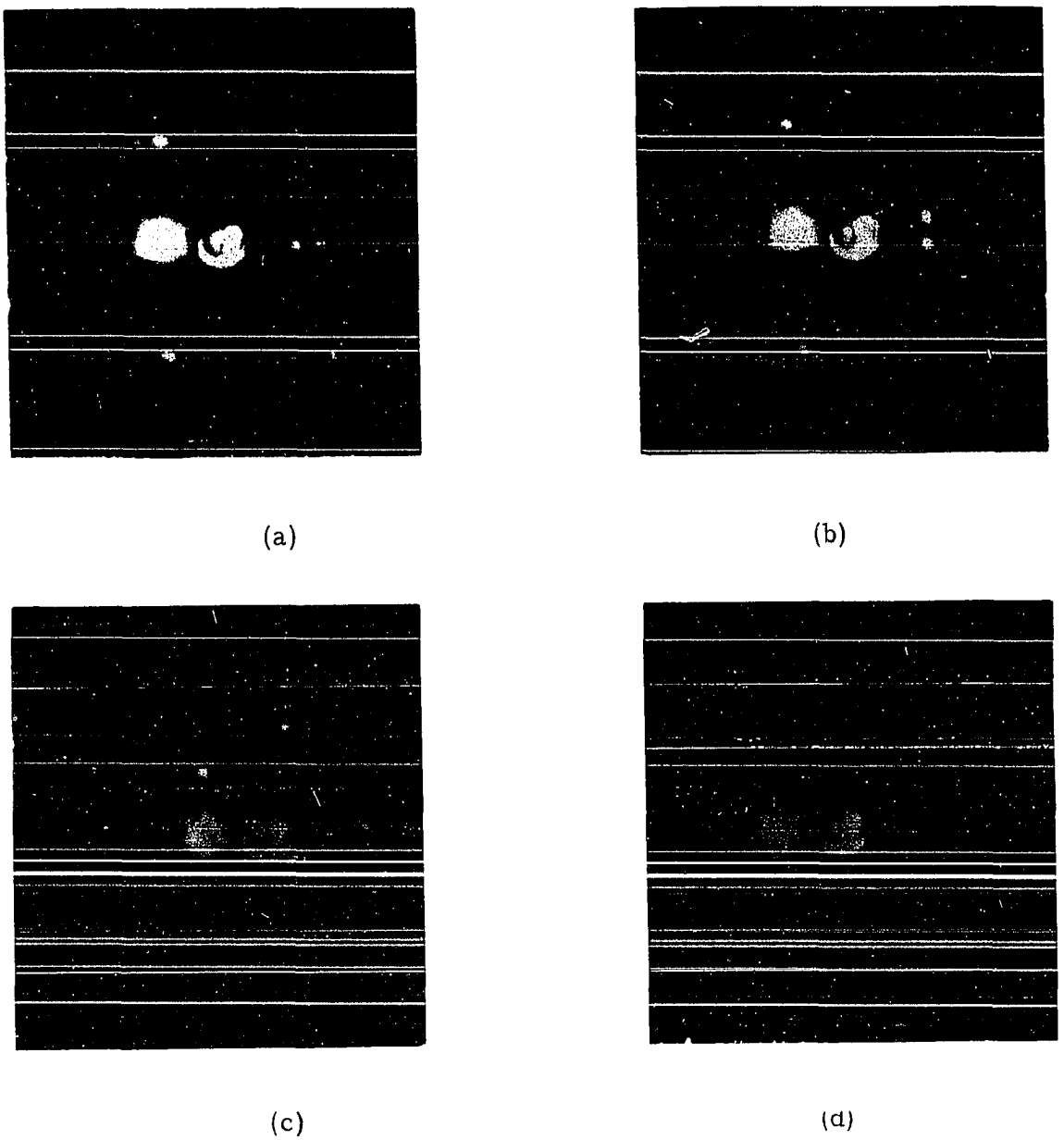

Fig. 13. LEED patterns resulting from the steady-state interaction of NO or O_2 with Ru(10$\bar{1}$0) at reactant partial pressures $\geq 10^{-8}$ torr, 38 eV beam energy, a) T = 950° C, b) T = 750° C, c) T $\geq$ 400° C and d) after cooling the surface shown in c) below 200° C in NO or O_2. These patterns are stable upon cooling below 200° C in vacuo.

about 0.6 monolayers with no apparent change in the LEED pattern. The rapid removal of weakly bound oxygen from the C(2x6) phase of the compound surface made the correlation between Auger data and LEED observations very difficult. In order to compensate for this effect, the O peak height was observed as a function of exposure to the incident beam and then was extrapolated to time zero. The extrapolation procedure was very important when an oxygenated surface was cooled below 200° C in the presence of NO gas since there was a 1:1 substitution of N for O adatoms with little or no change in the total adatom density. The apparent presence of nitrogen on these surfaces was a beam-induced artifact.

When a (2x1)+C(2x6) surface was cooled in either an NO or O_2 ambient, there was a gradual fading of the $\frac{1}{2}$ order beams, an increase in the background level and the eventual formation of the somewhat diffuse C(2x6) shown in Fig. 13d. The transition temperature ranged from -40 to 200° C and was a function of the fractional surface coverage of oxygen adatoms. This transition occurred at a higher temperature in an NO ambient than it did in O_2. Extrapolated Auger data for the C(2x6) surface showed that there was no N on the surface and that the O coverage ranged from slightly more than 0.5 up to 0.85 monolayers. The $\frac{1}{2}$ order reflections were regenerated by heating the sample above 200° C. This transition has been observed to occur with no apparent change in

surface coverage.

The ordered surface structures shown in Figs. 13a and 13b, i.e., (7x1) and C(4x8), have also been observed. The former structure was produced by flashing an oxygenated surface with $\theta > 0.2$ to 950° C in vacuo for several minutes. The latter LEED pattern has been observed both after steady-state interaction of the sample with either NO or O_2 at temperatures above 700° C and after flashing a (2x1), C(2x6) or (2x1)+ C(2x6) surface to 750° C in vacuo. Auger analysis did not detect the presence of nitrogen on either surface, and the maximum oxygen coverages were 0.47±.02 and 0.28±.02 monolayers, respectively.

When the (7x1) surface was exposed to either NO or O_2 at temperatures above 400° C, the diffraction pattern began to streak in the $\vec{k}$ direction. A C(4x8) pattern eventually formed. Continued exposure resulted in the concurrent fading of the C(4x8) spots and formation of C(2x6)+(2x1) reflections. If either structure was exposed to continued adsorption at temperatures below 400° C, a diffuse C(2x4) would begin to appear. The C(2x4) eventually transformed into a (2x1) resulting in either a (7x1)+(2x1) or C(4x8)+(2x1) compound surface.

The stability of the C(2x6)+(2x1) surface in a reducing atmosphere was examined. There was no noticeable change in the LEED pattern after the surface had been exposed to 5×10^{-7} torr of hydrogen for thirty minutes at temperatures below 300° C; however, when the

temperature was raised above 300° C, the pattern regressed through the C(4x8) and (7x1) structures before finally becoming a (1x1) with a high background. When another compound surface was exposed to a 3:1 mixture of H_2/NO, it remained stable at temperatures up to 400° C, but it decomposed fairly rapidly at 520° C. When a clean surface was exposed to the H_2/NO mixture, no ordered structures were formed, and the limiting surface coverage was about one half of a monolayer.

DISCUSSION OF RESULTS

Structures Resulting from the Interaction of Nitric Oxide and Oxygen with Ru(10$\bar{1}$0)

The qualitative nature of LEED observations based solely upon the positions of new diffraction features does not allow for an unambiguous assignment of atomic positions, and while only one model for each particular interaction will be considered, it must be borne in mind that in general several structural types could satisfy the individual diffraction results. The proposed surface structures account for the observed LEED patterns, are consistent with the Auger analyses and have some basis in the current literature. These models are ideal, two-dimensional overlayers, but if the trough-like nature of the substrate is considered, the different environments of atoms within the overlayers must cause their heights above an ideal hcp (10$\bar{1}$0) surface to vary. The existence of buckling of this sort would make itself manifest in altered intensities, but at the level of interpretation employed in this study it is quite impossible to draw any conclusions regarding such displacements. A definitive answer concerning the atomic arrangements in these surface structures could only be obtained from an analysis of the intensity data.

The C(2x4) and (2x1) surface structures were formed by rapid adsorption of either NO or O_2 at moderate temperatures. These surfaces have been extensively studied by KGB who concluded that they were

formed by the dissociative adsorption of the diatoms into the ordered arrays shown in Figs. 14a and 14b. The chemisorbed species sit in the simple potential minima of the substrate lattice as assumed in the classical approach to chemisorbed structures. It is not possible to ascertain the position of an adatom relative to the underlying substrate atoms, but Marcus, Demuth and Jepsen (50) have performed an intensity analysis of the Ni(100)-(2x1)-O structure. They found that the O atoms were in the two-fold bridge position directly above the short side of the rectangular unit cell at a distance of 1.45 Å above the plane passing through the center of the underlying Ni layer.

According to the KGB model, NO dissociatively adsorbs to form a C(2x4) surface at a coverage of one quarter of a monolayer of N and O atoms and a (2x1) array at a maximum coverage of one half of a monolayer. This model is the basis for relating relative Auger intensities to absolute coverages. The average maximum Auger peak height of either O (from an O_2 dose) or N plus O (from an NO dose) from twenty-five observations of the (2x1) surface was 40±2 arbitrary units. This peak-to-peak height was considered to correspond to one half of a monolayer of adsorbed atoms. This definition, along with the assumption that the peak height was a linear function of the surface coverage, was used to scale the data. This proportionality constant produced values of σ, the cross section for electron-stimulated desorption, and λ, the electron

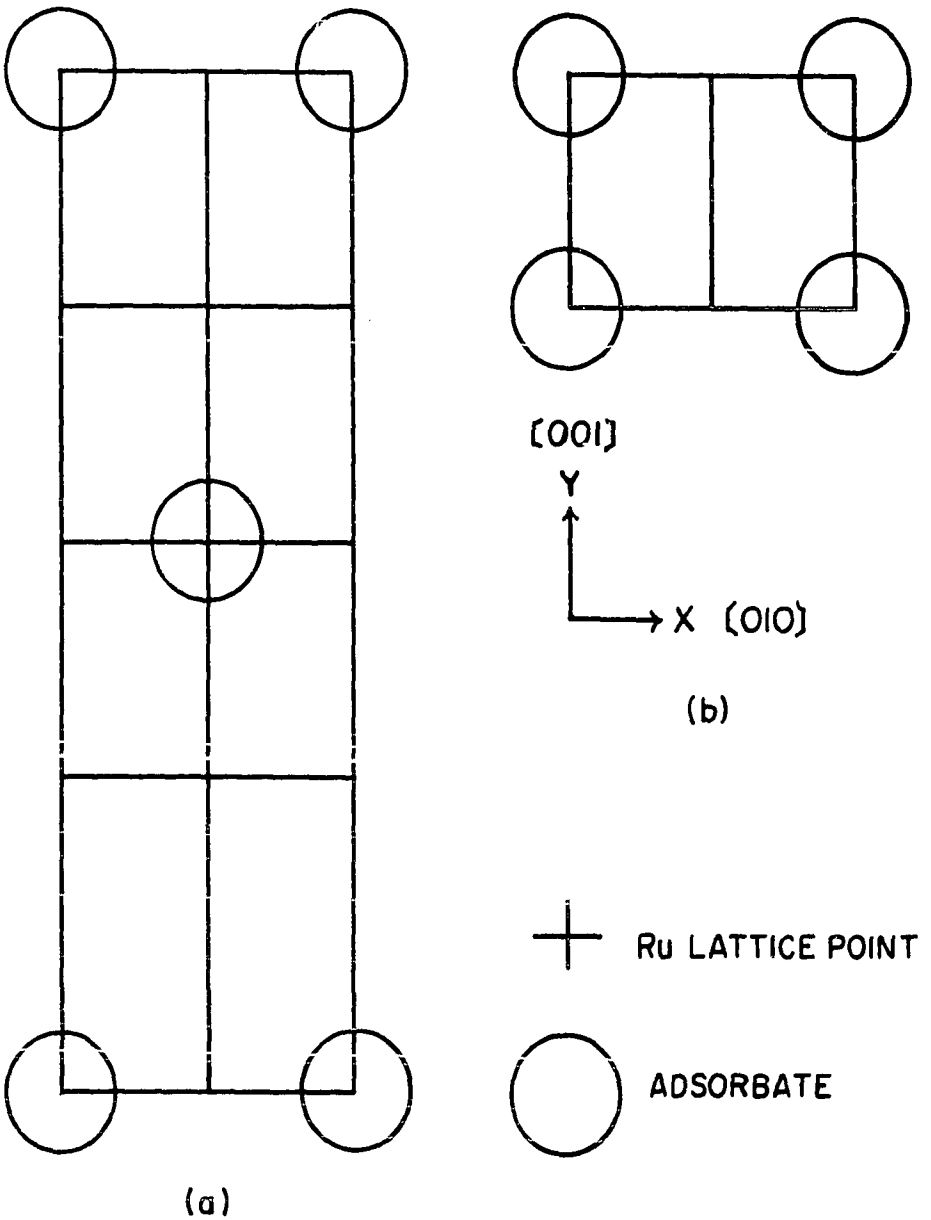

Fig. 14. Adsorbate overlayers due to NO or O_2 adsorption on Ru(10$\bar{1}$0) at T ≤ 200° C; a) doubly primitive centered-rectangular unit cell of C(2x4) overlayer and b) primitive unit cell of (2x1) overlayer.

escape depth, which are in reasonable agreement with accepted values, and it provided very good agreement between the adatom densities predicted by atomic models proposed for the ordered structures and those found by Auger analysis.

While this study does not provide sufficient data to develop a detailed microscopic model of the kinetics of formation of these structures, examination of Figs. 10 and 12 can provide some insight into the mechanism. The shapes of the fractional surface coverage versus exposure curves for NO and O_2 indicate that basically the same kinetics are applicable in both cases for coverages below 0.2; beyond this point the oxygen data show a decrease in the rate of adsorption. If the sticking probability is constant up to almost saturation coverage, it is then generally thought that the adsorption takes place via a weakly bound, highly mobile precursor state (74). Molecules in this state diffuse across the partially-covered surface until they either encounter unoccupied adsorption sites or desorb; as a result, the overall sticking probability will be determined by the relative rates of these two processes. Such precursor states have very short lifetimes on the surface at moderate temperatures, but they can diffuse appreciable distances during their adsorbed lifetime. The equilibrium coverage of such molecules is considered to be negligible compared to the chemisorbed layer.

In the case of NO adsorption, the precursor state may be the weakly chemisorbed molecular state observed by KGB. The heat of adsorption should be sufficiently large to insure that essentially every impinging NO molecule is trapped at the surface and enters this precursor state. These molecules would then diffuse to sites where they can dissociate and become strongly chemisorbed. KGB presented evidence that indicated, once the NO bond was broken, additional diffusion resulted in the segregation of the adatoms into separate patches of N and O. They did not propose the existence of two different types of adsorption sites but only that the preference of each dissociated species for like neighbors was sufficient driving force to result in segregation. It should be noted that this segregation of like adatoms into patches is not the only explanation that is consistent with the results of KGB and that the conclusions based on this study are not dependent upon this type of adatom rearrangement. However, the appearance of ordered LEED structures long before saturation coverage was reached does indicate that the adatoms tend to form islands even in the limit of very low coverage.

The oxygen data began to deviate from the NO results upon completion of the C(2x4) structure. This may have occurred because no chemisorbed molecular state for O_2 similar to the one for NO has been found; as a result, the oxygen precursor state should be much more weakly bound

than the NO precursor. If once the surface is covered with the ordered C(2x4) overlayer, the heat of adsorption of molecular oxygen in the precursor state drops, then the activation energy necessary to pass from the precursor state to the chemisorbed state may become greater than the activation energy for desorption from the precursor state. In this circumstance chemisorption becomes activated, and the nucleation of the (2x1) surface structure would be a slow process. Precursor molecules must migrate large distances before encountering the edge of a (2x1) island, and only those molecules adsorbed within a characteristic migration distance of the island edges become strongly chemisorbed. As the islands grow, the perimeters expand, and the sticking coefficient begins to increase. As the coverage continues to increase, the vacant troughs on the C(2x4) surface become occupied; these troughs which are nearly filled, but still staggered with respect to one another, begin to align by diffusion. This would cause the $\frac{1}{4}$ order reflections to merge into $\frac{1}{2}$ order spots. The uptake of oxygen at temperatures below 200° C ceases with the completion of the (2x1) structure because there are no molecular adsorption states and because the occupation of the vacant sites along the troughs in the (2x1) surface is energetically unfavorable since the resultant O-O separation distance (2.71 Å) would be less than the diameter of an O^{2-} ion (2.8 Å).

The (7x1), C(4x8) and C(2x6) surfaces were formed only after long

exposures to either NO or O_2 at elevated temperatures. All of these surfaces are modeled as coincident lattices in which most of the atoms lie in positions of low symmetry with respect to the underlying substrate. The coincident lattice model (75) involves the placement of a simple uniform overlayer structure upon a known substrate geometry. The basic assumption is that the atoms in the surface layer interact with one another in such a manner as to form an overlayer structure that in general ignores the two-dimensional periodicity of the substrate, and, as a result, atoms in the surface overlayer may not always reside on substrate sites of high symmetry that tend to maximize the bonding coordination of the surface to substrate atoms. In such models there is only an occasional coincidence between lattice points of the surface and substrate structures. The existence of such overlayers was confirmed by the first analysis of LEED intensities. Tucker and Duke (76), who used data-reduction and kinematical concepts, found that a Rh(100)-C(2x8)-O structure was indeed a coincident lattice.

One possible atomic configuration that would account for a C(2x6) LEED pattern is shown in Fig. 15. The oxygen adatoms form a hcp array that is compressed ($\alpha = 93°$; $\beta = 133°$) along the direction of the troughs. The overlayer is rather loosely packed with the smallest O-O distance equal to 3.73 Å. Sensible deviations from the coincident lattice configuration and high chemical activity could be expected to result from

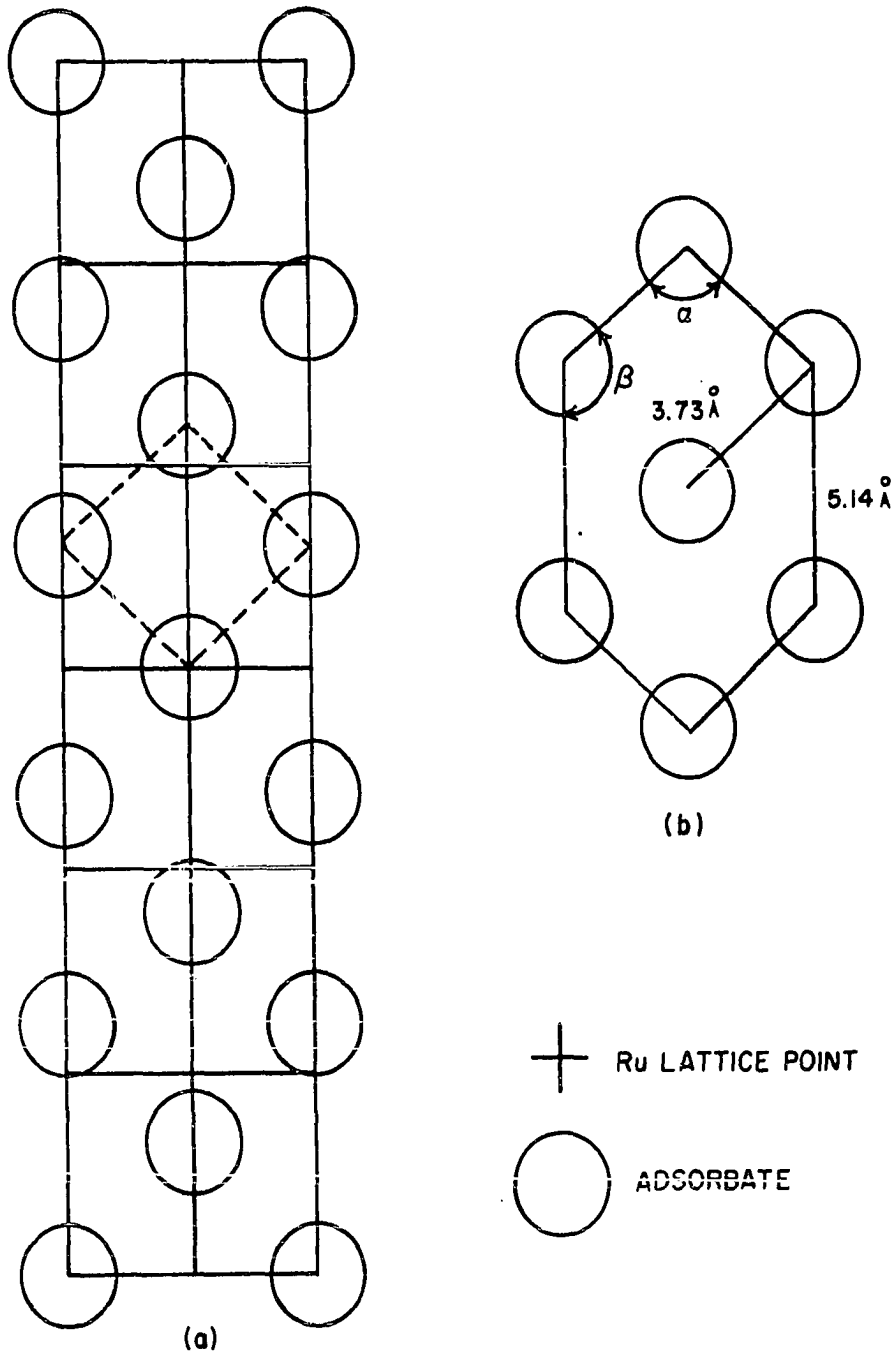

Fig. 15. Oxygen overlayer due to NO or O_2 interaction with Ru(10$\bar{1}$0); a) nonprimitive centered-rectangular unit cell of C(2x6) overlayer (the dashed lines indicate the primitive unit cell) and b) compressed hcp array of oxygen adatoms.

the rather open structure. The lack of registry between the overlayer and substrate in this model for the C(2x6) could produce variations in the bonding with the most weakly bound O on those sites furthest removed from registry. This variation in the bonding would account for the rapid initial drop in surface coverage when a surface containing regions of C(2x6) structure is either exposed to the Auger beam or evacuated. The ideal model coverage of 5/6 or 0.83 corresponds to the experimentally observed maximum coverage of 0.80±.05.

This particular overlayer was originally proposed by Tucker (77, 78) for a C(2x6)-O overlayer on Rh(110). The (110) face of a fcc metal is similar to a hcp $(10\bar{1}0)$ plane, but they differ in the coordination numbers of the surface and second-layer atoms. Tucker based his conclusions upon a qualitative consideration of the variations of the intensities of the fractional order beams with incident beam energy. He positioned the oxygen layer on top of the substrate atoms. The adatom density was not measured experimentally. A C(2x6)-O has also been observed on Cu(110) (79), but no coverage measurements were made, and no model was proposed.

A minimum temperature of formation of over 400° C and an estimated sticking coefficient of less than 0.05 indicate that there is a considerable activation barrier to the nucleation of C(2x6) islands on a (2x1) surface. The barrier to continued adsorption into the C(2x6) phase at elevated

temperatures increases with coverage until it eventually becomes greater than the activation energy for desorption from the precursor state thus effectively preventing the completion of the C(2x6) structure on a laboratory time scale. Under steady-state conditions the surface is covered with a mixture of C(2x6) and (2x1) domains. The individual patches have areas on the order of 10^4 Å^2 or more since the diffraction pattern is a superposition of the spots belonging to each of the structures which indicates that the patches are larger than the coherence width of the incident beam, i.e., each domain scatters electrons independently and the intensity contributions from the individual regions add together to form the resultant diffraction pattern. If the substrate temperature is reduced below 200° C, the rate of desorption from the precursor state decreases, and the surface eventually becomes completely covered with the C(2x6) phase. The faster disappearance of the (2x1) in an NO ambient than in O_2 is consistent with the proposed precursor state model.

The coexistence of two structurally different surface phases at elevated temperatures has been observed for the O_2/Ni(110) system. An oxide overlayer formed on the Ni(110) surface at room temperature (80). The overall repeating mesh of the surface structure was (9x4), and the "pseudo-oxide" plane closely resembled the (100) face of NiO. When this pseudo-oxide was heated, an irreversible disproportionation into islands of proper NiO surrounded by (2x1)-O structure occurred.

The presence of two oxygen species on a Ru surface has been confirmed by the work of Kim and Winograd (81). Their XPS study of Ru powder exposed to 100 torr of O_2 for three hours showed that oxygen uptake ceased below the amount necessary for the formation of RuO_2. Two O_{1s} peaks separated by 1.6 eV were present in the spectrum. The lower energy peak was attributed to oxygen below the surface, perhaps RuO, while the high energy peak was assigned to chemisorbed atomic O. Two forms of adsorbed oxygen were clearly present but a more explicit description of the structural differences was not possible from the XPS data alone.

A possible adatom overlayer that would produce a C(4x8) LEED pattern is shown in Fig. 16. The C(4x8) is very similar to the (2x1). It can be formed from the (2x1) by removing about 7% of the adatoms and by shifting every other column of adatoms in a direction perpendicular to the troughs. In fact a C(4x8) can be produced by flashing a (2x1) surface to 750° C in vacuo. Since oxygen can be removed from the surface by holding the sample at 650° C overnight in vacuo, the Ru-O bond must be rather weak at these temperatures, and it seems reasonable that the long-range Coulomb repulsions between the electronegative O atoms would force the adatoms farther apart. The nearest-neighbor distances in the C(4x8) are about 10% larger than in the (2x1). The predicted coverage of 7/16 or 0.438 is in good agreement with the observed

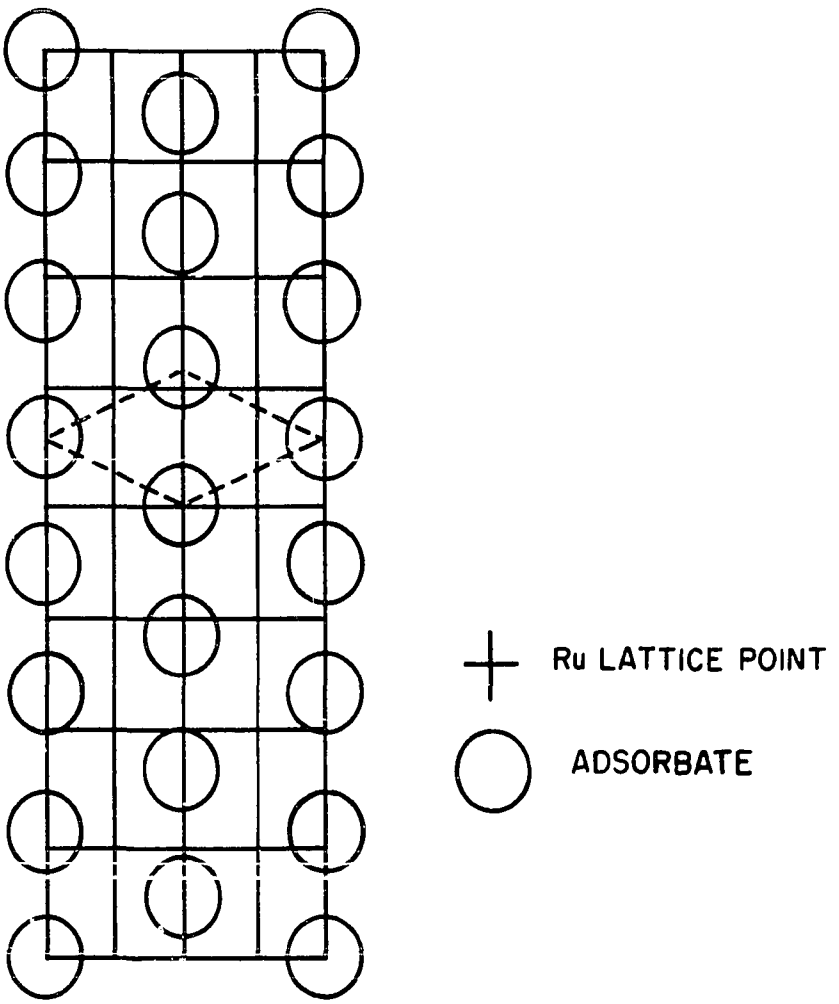

Fig. 16. Nonprimitive centered-rectangular unit cell of the C(4x8) oxygen overlayer due to NO or O_2 interaction with Ru(10$\bar{1}$0) at 750° C. The dashed lines indicate the primitive unit cell of the overlayer.

coverage of 0.47±.02.

The proposed (7x1) overlayer shown in Fig. 17 is most likely formed by either a number of adsorption/desorption steps with random recombination of the adatoms or by highly mobile adatoms with large repulsive interactions. The temperature necessary to form this structure

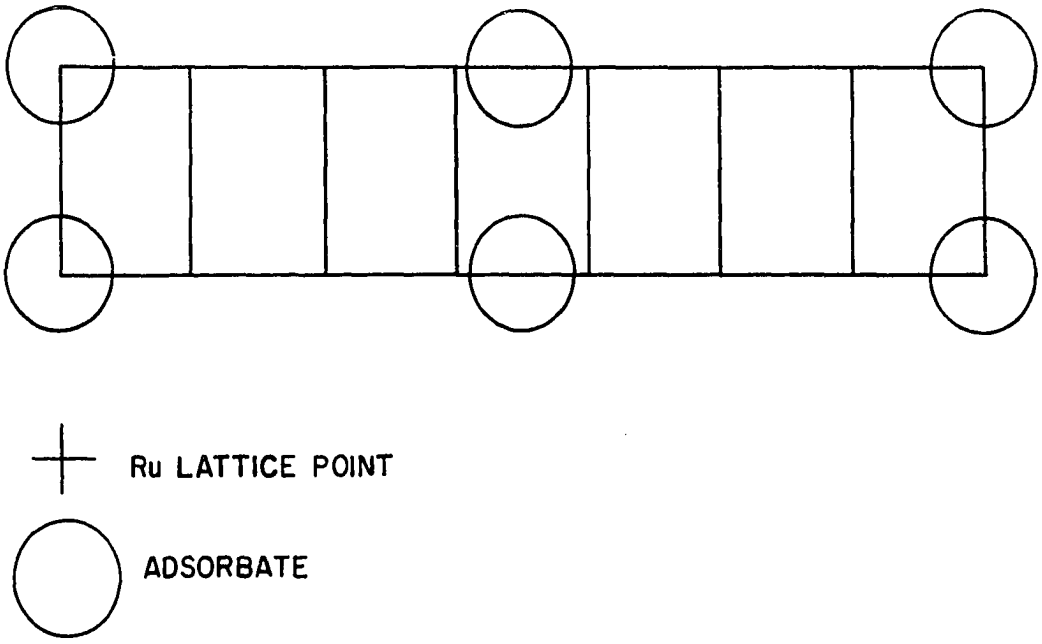

Fig. 17. Doubly primitive unit cell of the (7x1) oxygen overlayer due to NO or O_2 interaction with Ru(10$\bar{1}$0) at 950° C.

correlates with the observed temperature of 930° C for the onset of oxygen desorption from an Ru field-emitter tip (73) and with the thermal desorption results of KGB and Madey et al. (10) which showed no oxygen desorption below 900° C and only partial desorption at temperatures near 1000° C. The predicted coverage of 2/7 or 0.286 is in excellent agreement with the observed coverage of 0.28±.02.

The LEED/AES results for the O_2/Ru system are summarized in Table 1. The results for the NO/Ru system are identical except that the C(2x4) and (2x1) surfaces have equal amounts of adsorbed N and O atoms when the substrate temperature is less than 200° C. The proposed

Table 1. Overlayer structures resulting from the interaction of O_2 with Ru(10$\bar{1}$0)

Structure	lattice type	θ^{max}_{exp}	θ^{max}_{model}	$T^{min}_{formation}$(°C)
C(2x4)	simple	0.25±.02	0.25	-25
(2x1)	simple	0.50±.02[a]	0.50	-25
C(2x6)	coincident	0.80±.05	0.83	400[b]
C(4x8)	coincident	0.47±.02	0.43	600
(7x1)	coincident	0.28±.02	0.29	>900

[a] By definition.

[b] Only observed after cooling a C(2x6)+(2x1) below 200°C in NO or O_2.

models for the low-temperature LEED patterns are characterized by the fact that all of the adatoms are in equivalent sites of high symmetry with respect to the substrate, while the remaining patterns have been modeled as coincident lattices in which most of the adatoms lie in positions of low symmetry. There is a considerable body of experimental evidence which indicates that there is a fundamental difference in the bonding of the oxygen adatoms to the surface between the simple and the coincident lattices. The simple lattices were formed by rapid adsorption of NO or O_2 at temperatures as low as -25°C, while the coincident lattices were characterized by sticking coefficients that were an order of magnitude

smaller and by minimum temperatures of formation between 400 and 900° C. The transition from a simple to a coincident lattice was irreversible, i.e., once a coincident lattice had been formed from a simple lattice by continued adsorption or by heating the surface, the resultant coincident lattice never reverted to a simple structure. On the other hand, transitions between the two simple lattices or among the three coincident lattices were reversible, e.g., a C(4x8) could be produced from a (7x1) surface by adsorption of NO at temperatures between 400 and 650° C, while the (7x1) could be regenerated either by flashing the C(4x8) to 950° C in vacuo or by exposing the C(4x8) to H_2 at elevated temperatures.

Even though the proposed atomic models for the coincident lattices do not require any rearrangement of the top layer of metal atoms in order to be able to satisfactorily account for the LEED data and the relative surface coverages determined by AES, these models do not provide any insight into possible reasons for either the appreciable activation energy necessary for the formation of these structures or the stability of these surfaces once they have been formed. The formulation of these lattices as two-dimensional, nonstoichiometric surface oxide phases formed by the incorporation of oxygen adatoms in a reconstructed layer of metal atoms can account for these observations. The LEED data do not exclude the possibility of surface reconstruction since, if

the rearranged surface atoms form an array having the same symmetry with respect to the underlying metal atoms as the overlayer, this reconstruction would cause only variations in diffracted intensities and would not cause the appearance of new fractional-order beams.

One possible configuration of surface atoms that would have C(2x6) symmetry with respect to the substrate is shown in Fig. 18b. This array is the asymmetric unit of the reconstructed surface; the nonprimitive rectangular unit cell of the C(2x6) surface is formed by reflection of the asymmetric unit throught the mirror plane which passes through the centers of the atoms in the top row. This structure is formed by shifting the surface atoms in the two center rows of Fig. 18a from the four-fold holes formed by the underlying metal atoms to the adjacent three-fold holes which are only 1.6 Å away. This reconstruction is accomplished without any change in the density of surface atoms. The reduction in metal-metal coordination accompanying reconstruction is counterbalanced by an increase in metal-adatom interactions. The average metal-metal distance in this layer is 3.29 Å which is only 6% smaller than the average distance in the unreconstructed layer.

One possible transition state that would lead to the formation of a C(2x6) by the reconstruction of a (2x1)-O is shown in Fig. 18c. The oxygen adatoms in the (2x1) have been placed in the two-fold bridge positions over the short side of the substrate unit cell. This is the

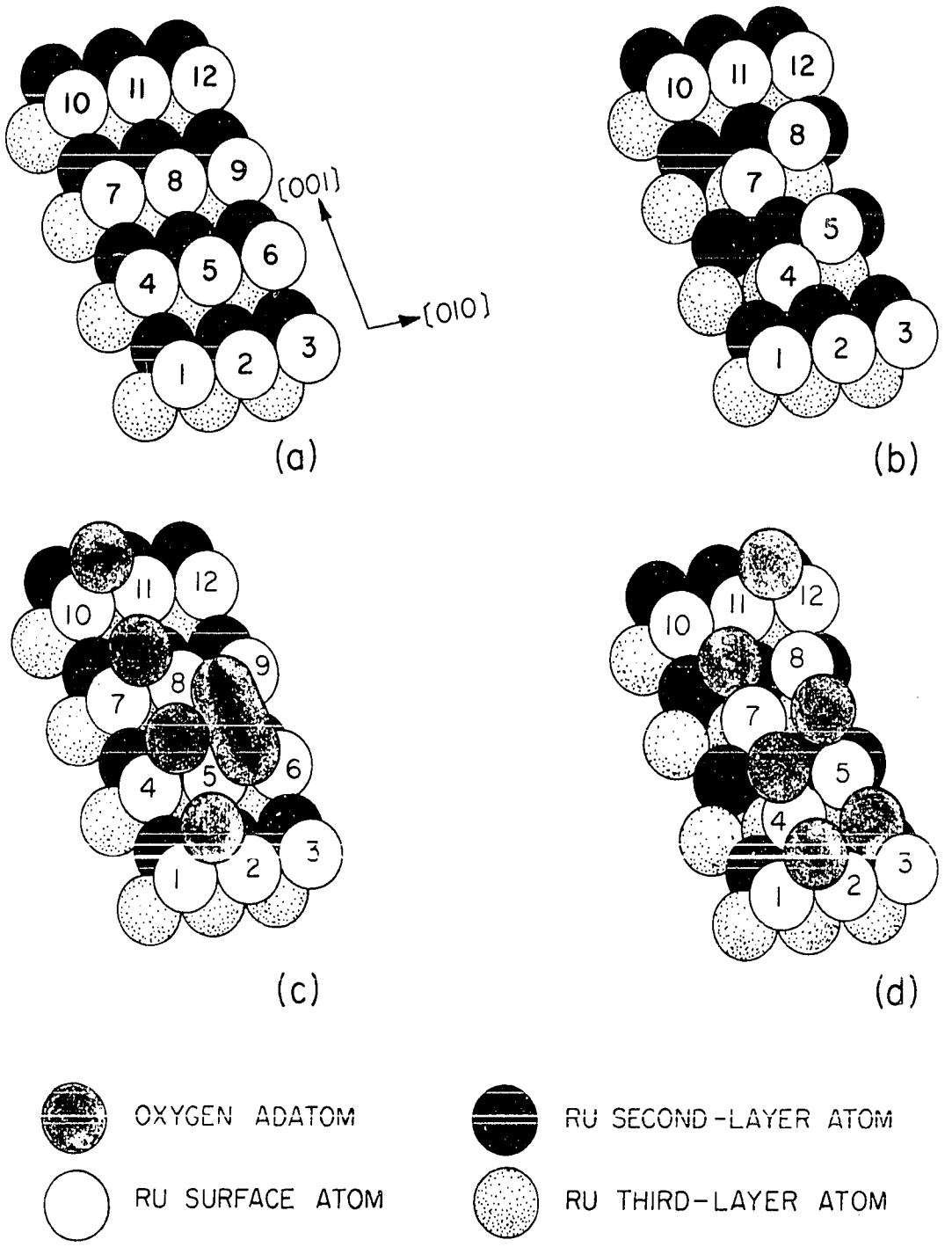

Fig. 18. C(2x6) oxide overlayer formed by the reconstruction of a Ru(10$\bar{1}$0) surface; a) ideal Ru(10$\bar{1}$0) surface, b) asymmetric unit of the reconstructed metal surface, c) transition state complex leading to the formation of a C(2x6)-O from a (2x1) surface and d) the asymmetric unit of the oxide phase.

atomic configuration proposed by Marcus et al. (50) for Ni(110)-(2x1)-O. The transition state complex is formed when one of the vacant columns in the (2x1) surface is occupied by an O_2 molecule. If the O-O bond happens to stretch in the [001] direction at the same time that the adjacent Ru and O atoms are moving in the directions indicated by the arrows in Fig. 18c, then it is possible that the O-O bond will break, the surface atoms will shift and the C(2x6) structure shown in Fig. 18d will be formed. Since a large number of atoms are involved in the transition state complex and since the lifetimes of oxygen molecules on the surface at elevated temperatures are expected to be very short, the probability that this concerted step will occur is very small. Since several bonds must be broken and some surface atoms must be displaced, the activation energy should be fairly large. Once the C(2x6) phase has nucleated, the activation energy should decrease. The ideal reconstructed overlayer has atoms that are only 1.6 Å from atoms in the unreconstructed surface. This distance is much less than the nearest-neighbor distance of 2.71 Å; as a result, atoms near the phase boundaries must be forced out of their equilibrium positions resulting in a large amount of local strain. This strain reduced the activation energy necessary for the continued growth of the C(2x6) phase along the [010] direction. This mechanism for the nucleation and growth of the oxide phase would result in the formation of large domains.

The atomic model originally proposed for the C(2x6)-O overlayer (see Fig. 15) is a planar array with oxygen atoms at (0, 0), (0, 5.14) and (0, 10.28). If the adatom at the origin is placed in the bridge position between Ru(1) and Ru(2) in Fig. 18b, the adatom at (0, 5.14) would nearly be centered between Ru(4) and Ru(7); in fact, the adatom is only 0.44 Å from the bridge position. The minimum distance between an O^{2-} ion and a Ru atom should be approximately equal to one half of the sum of the diameter of the ion and the nearest-neighbor distance in the metal or about 2.75 Å. In order for the adatom to be 2.75 Å from Ru(4) and Ru(7), it must be 1.73 Å above the plane passing through the centers of the metal atoms. This adatom is effectively bridge bonded to the surface since the next nearest metal atom is Ru(5) which is at a distance of 3.22 Å. The overlayer oxygen adatom at (0, 10.28) is less than 0.2 Å from the center of the triangle formed by Ru(7)-Ru(10)-Ru(11). This opening is sufficiently large to allow an O^{2-} ion to penetrate the surface and bridge bond to two second-layer metal atoms. This adatom would be almost coplanar with the top layer of metal atoms. It would be expected to be very strongly bound since it is 2.74 Å from Ru(7), Ru(10) and Ru(11) and 2.91 Å from Ru(8).

This reconstruction model for the C(2x6)-O structure provides reasonable explanations for the experimental observations. The number of oxygen adatoms per unit cell agrees with the AES results, and these

adatoms are in bonding sites that maximize the oxygen-metal interaction and that are within 10% of the positions calculated from the LEED data. This model predicts both a large activation energy and island growth. Neither long-range migrations of surface atoms nor transport of atoms between the bulk and surface regions are necessary.

A considerable amount of supporting evidence for this surface oxide model can be found in the recent literature. One of the more convincing pieces of this evidence is the XPS/UPS study of the O_2/Ni system by Norton and Tapping (82). The adsorption of oxygen on Ni foils was characterized by two kinetic regions. In the first ($\theta \leq 0.4$) it was established that chemisorption occurred with little change in the core and valence spectra which indicated that the surface metal atoms retained their metallic character. In the range $0.5 \leq \theta \leq 2.0$ the core and valence level spectra reflected the occurrence of oxide nucleation and finally the formation of a passive film of NiO.

Several other studies have found indirect evidence for the formation of surface oxides among the Group VIII metals. Ducros and Merrill (83) did a LEED/AES study of O_2 on Pt(110) and found that at temperatures above 800° C oxygen produced an elongated C(2x2) LEED pattern which was attributed to a transition oxide that led eventually to the epitaxial growth of PtO. The PtO overlayer did not react with H_2 or CO and decomposed above 1000° C. The interactions of O_2 with Ir(111) (84) and

Ru(0001) (10) have also been studied. Both surfaces have hexagonal symmetry and exhibited (2x2) LEED patterns after exposure to O_2 at room temperature. Both teams of investigators attributed the observed pattern to three degenerate domains of (2x1) symmetry. According to this model, an ideal surface would have a coverage of one half of a monolayer, but in both cases adsorption was observed to continue beyond this point with no change in the LEED pattern.

Ivanov et al. (84) found a peak in their thermal desorption spectra of oxygen from Ir(111) at 1270 K. They concluded that this feature was not due to desorption of oxygen from the ordered overlayer that produced the (2x2) LEED pattern; rather it represented desorption from a nonstoichiometric oxide in the near-surface region. This surface oxide had a minimum temperature of formation around 400° C, decomposed near 1000° C and exhibited a (1x1) LEED pattern. The (2x2) pattern was the same whether the oxide was present or not.

The adsorption data of Madey et al. (10) for Ru(0001) seemed to indicate clearly that there were at least two modes of oxygen bonding to the surface. There was a distinct change in the surface dipole moment per adsorbed species at $\theta \approx 0.5$, at precisely the same coverage at which the LEED intensity reached its maximum value. In addition, the temperature dependence of the LEED intensities was different for $\theta \approx 0.5$ and $\theta \approx 1.0$. They proposed the formation of a RuO_2 overlayer with

(2x2) symmetry to explain these results, but they did not rule out the possibility of surface reconstruction.

The Relationship Between the Observed Structures and the Results of Previous Investigations

The results of this investigation suggest a possible reason for the reported (2-4, 6) dual state behavior of supported Ru catalysts. Taylor et al. (4) observed a reversible conversion of their Ru catalyst between two activity states. The oxidized form was produced by treating the catalyst with either O_2 at 200° C or NO at 300° C. The reduced state was regenerated by exposing the oxidized form to H_2 or CO at temperatures above 650° C. Hydrogen chemisorption studies showed that the reduced and oxidized forms contained 0.6 and 0.8 monolayers of oxygen, respectively. These two states exhibited about the same activity for the reduction of NO to N_2, but they differed in their activity for ammonia decomposition and hydrocarbon formation from CO and H_2. The oxidized form was active, while the reduced catalyst was basically inert.

The oxidized form of a supported Ru catalyst resembles the C(2x6)-O oxide phase observed in this study. They both exhibit minimum temperatures of formation, are stable in reducing atmospheres at moderate temperatures and have oxygen coverages in the submonolayer range. The geometrical configuration and electronic structure of the reconstructed oxide layer shown in Fig. 18d are different than those of the bare metal,

and these differences should result in a difference in catalytic activity. Since some of the oxygen adatoms are incorporated in the reconstructed metal surface, chemisorption may take place on either the metal atoms or the oxygen atoms. The activity of the oxidized catalyst for ammonia decomposition and hydrocarbon formation may be related to the ability of the oxygen adatoms to form hydroxyl groups with adsorbed hydrogen. On the other hand, the two forms of the catalyst would be expected to have about the same activity for the reduction of NO to N_2 if the rate of this reaction depended solely upon the ability of a catalyst to adsorb NO dissociatively.

Since the kinetic studies were done under much more drastic experimental conditions, i.e., at much higher pressures and with multi-component feed streams, it is not expected that the surface oxide formed under those conditions would correspond exactly with the observed C(2x6)-O phase. If the oxidized form of the catalyst does have a reconstructed surface, then the reduced form would have an unreconstructed surface with a disordered oxygen overlayer. There was no indication of surface contamination by the nitrogen-containing layer proposed by Voorhoeve and Trimble (60) to account for dual state behavior. It is possible that this layer does not form to an appreciable extent under the milder experimental conditions used in this study; however, the presence of nitrogen on a reduced Ru catalyst has not been verified experimentally;

as a result, it is also possible that such a layer does not exist.

A variation in chemisorption properties with surface structure has been observed by Helms, Bonzel and Kelemen (85) for a Pt(100) surface. The clean surface can exist in one of two geometries depending upon the method used to clean it. The surface atoms can occupy the normal bulk positions, or they can reconstruct to form a surface which exhibits a (5x20) LEED pattern. The (5x20) has been interpreted as being due to the formation of a hexagonal, closepacked overlayer on the otherwise unperturbed lattice. There was a three order of magnitude difference in the sticking coefficients of H_2 and O_2 between the unreconstructed surface which was active and the (5x20) which was inert.

FUTURE INVESTIGATIONS

This investigation has shown that the interaction of Ru(10$\bar{1}$0) with nitric oxide or oxygen resulted in the formation of a number of different surface structures. There was a considerable amount of indirect evidence that indicated the existence of two distinct bonding modes of oxygen to the surface. It would appear advantageous to correlate this study with photoelectron spectroscopic measurements in hopes of obtaining more direct information on the electronic structure of the adsorbed complexes. It has been amply demonstrated that x ray induced photoelectron spectroscopy (XPS, also known as ESCA) yields information on both core levels (energy relative to the Fermi level and photoemission intensity) and valence levels, while ultraviolet photoelectron spectroscopy (UPS) can probe the valence region with increased sensitivity and resolution. These techniques can be applied to adsorbate systems. The determination of the relationship between the fractional surface coverage of an adsorbate and the changes in the XPS and UPS spectra may verify the existence of a surface oxide layer. In situ use of a LEED system would provide a firm basis for comparison between data obtained by these methods and those obtained in this study.

BIBLIOGRAPHY

1. M. Shelef and H. Gandhi, Ind. Eng. Chem. Prod. Res. Develop., 11, 393 (1972).

2. R. L. Klimisch and K. C. Taylor, Envir. Sci. & Tech., 7, 127 (1973).

3. K. C. Taylor and R. L. Klimisch, J. Catal., 30, 478 (1973).

4. K. C. Taylor, R. M. Sinkevitch and R. L. Klimisch, J. Catal., 35, 34 (1974).

5. T. P. Kobylinski and B. W. Taylor, J. Catal., 33, 376 (1974).

6. R. L. Klimisch and K. C. Taylor, Ind. Eng. Chem. Prod. Res. Develop., 14, 26 (1975).

7. J. T. Grant and T. W. Haas, Sur. Sci., 21, 76 (1970).

8. R. Ku, N. A. Gjostein and H. P. Bonzel, in Catalytic Chemistry of Nitrogen Oxides, edited by R. L. Klimisch and J. G. Larson (Plenum Press, New York, N. Y., 1975).

9. H. P. Bonzel and T. E. Fischer, Sur. Sci., 51, 213 (1975).

10. T. E. Madey, H. A. Engelhardt and D. Menzel, Sur. Sci., 48, 304 (1975).

11. J. C. Fuggle, T. E. Madey, M. Steinkilberg and D. Menzel, Sur. Sci., 52, 521 (1975).

12. P. Auger, J. Phys. Radium, 6, 205 (1925).

13. G. Wentzel, Z. Physik, 43, 524 (1927).

14. E. H. S. Burhop, The Auger Effect and Other Radiationless Transitions (Cambridge Univ. Press, Cambridge, England, 1952).

15. E. H. S. Burhop and W. N. Asaad, Adv. in Atomic and Molecular Phys., 8, 163 (1972).

16. J. J. Lander, Phys. Rev., 91, 1382 (1953).

17. L. A. Harris, J. App. Phys., 39, 1419 (1968).

18. R. E. Weber and W. T. Peria, J. App. Phys., 38, 4355 (1967).

19. P. W. Palmberg, G. K. Bohn and J. C. Tracy, App. Phys. Lett., 15, 254 (1969).

20. C. B. Duke, CRC Critical Reviews in Solid State Science, 4, 371 (1974).

21. L. B, Leder and J. A. Simpson, Rev. Sci. Instr., 29, 571 (1958).

22. N. J. Taylor, Rev. Sci. Instr., 40, 792 (1969).

23. C. C. Chang, in Characterization of Solid Surfaces, edited by P. F. Kane and G. B. Larrabee (Plenum Press, New York, N. Y., 1974).

24. R. L. Park, J. E. Houston and G. E. Laramore, Proc. 2nd Internl. Conf. on Solid Surfaces, 757 (1974).

25. C. D. Wagner, Faraday Disc. of Chem. Soc., 60, 291 (1975).

26. T. W. Haas, J. T. Grant and G. J. Dooley, in Adsorption-Desorption Phenomena, edited by F. Ricca (Academic Press, New York, N.Y., 1972).

27. M. P. Hooker and J. T. Grant, Sur. Sci., 55, 741 (1976).

28. J. T. Grant and M. P. Hooker, Solid State Comm., 19, 111 (1976).

29. R. L. Park and J. E. Houston, J. Vac. Sci. & Tech., 11, 1 (1974).

30. W. M. Mularie and W. T. Peria, Sur. Sci., 26, 125 (1971).

31. T. E. Gallon, J. Phys. D, 5, 822 (1972).

32. H. E. Bishop and J. C. Riviere, J. App. Phys., 40, 1740 (1969).

33. C. R. Brundle, J. Vac. Sci. & Tech., 11, 212 (1974).

34. C. J. Powell, Sur. Sci., 44, 29 (1974).

35. R. E. Weber and A. L. Johnson, J. App. Phys., 40, 314 (1969).

36. E. N. Sickafus, J. Vac. Sci. & Tech., 11, 299 (1974).

37. P. W. Palmberg, J. Vac. Sci. & Tech., 13, 214 (1976).

38. C. J. Davisson and L. H. Germer, Phys. Rev., 30, 705 (1927).

39. D. L. Summers, Ph. D. Thesis, Iowa State University (1974).

40. C. B. Duke, Proc. 2nd Internl. Conf. on Solid Surfaces, 641 (1974).

41. J. B. Pendry, Low Energy Electron Diffraction (Academic Press, London, 1974).

42. K. Kambe, Proc. 2nd Internl. Conf. on Solid Surfaces, 607 (1974).

43. C. B. Duke, Adv. in Chem. Phys., 27, 1 (1974).

44. M. B. Webb and M. G. Lagally, Solid State Phys., 28, 301 (1973).

45. J. E. Demuth, D. W. Jepsen and P. M. Marcus, Phys. Rev. Lett., 31, 540 (1973).

46. C. B. Duke, N. O. Lipari, G. E. Laramore and J. B. Theeten, Solid State Comm., 13, 579 (1973).

47. S. Andersson, D. Kasemo, J. B. Pendry and M. A. Van Hove, Phys. Rev. Lett., 31, 595 (1973).

48. C. B. Duke and N. O. Lipari, J. Vac. Sci. & Tech., 12, 222 (1975).

49. M. Van Hove and S. Y. Tong, J. Vac. Sci. & Tech., 12, 230 (1975).

50. P. M. Marcus, J. E. Demuth and D. W. Jepsen, Sur. Sci., 53, 501 (1975).

51. C. B. Duke, N. O. Lipari and G. E. Laramore, Nuovo Cimento, 23B, 241 (1974).

52. M. Shelef, K. Otto and H. Gandhi, Atmos. Envir., 3, 107 (1969).

53. E. R. S. Winter, J. Catal., 22, 158 (1971).

54. S. Sourirajan and J. L. Blumenthal, Internl. J. Air & Water Poll., 5, 24 (1961).

55. J. H. Jones, J. T. Kummer, K. Otto, M. Shelef and E. Weaver, Envir. Sci. & Tech., 5, 790 (1971).

56. R. L. Klimisch and G. J. Barnes, Envir. Sci. & Tech., 6, 543 (1972).

57. M. Shelef and H. Gandhi, Ind. Eng. Prod. Res. Develop., 13, 80 (1974).

58. M. Shelef and H. Gandhi, Ind. Eng. Prod. Res. Develop., 11, 2 (1972).

59. K. Otto and M. Shelef, Z. Phys. Chem. (Frankfurt am Main), 85, 308 (1973).

60. R. J. H. Voorhoeve and L. E. Trimble, J. Catal., 38, 80 (1975).

61. F. A. Cotton and G. Wilkinson, Advanced Inorganic Chemistry, 3rd ed., p. 1012 (John Wiley and Sons, Inc., New York, N. Y., 1972).

62. J. J. Brophy, Basic Electronics for Scientists, p. 271 (McGraw-Hill Book Company, New York, N. Y., 1966).

63. L. McDonnell, B. D. Powell and D. P. Woodruff, Sur. Sci., 40, 669 (1973).

64. G. E. Becker and H. D. Hagstrum, J. Vac. Sci. & Tech., 11, 284 (1974).

65. G. E. Laramore, Phys. Rev. B, 6, 1097 (1972).

66. C. B. Duke and G. E. Laramore, Phys. Rev. B, 2, 4783 (1970).

67. J. C. Tracy and J. M. Burkstrand, CRC Critical Reviews in Solid State Science, 4, 380 (1974).

68. F. A. Cotton and G. Wilkinson, Advanced Inorganic Chemistry, 3rd ed., p. 1010 (John Wiley and Sons, Inc., New York, N. Y., 1972).

69. S. Usami and T. Nakagima, Proc. 2nd Internl. Conf. on Solid Surfaces, 237 (1974).

70. H. Conrad, G. Ertl, J. Kuppers and E. Latta, Sur. Sci., 50, 296 (1975).

71. R. G. Musket, Sur. Sci., 21, 440 (1970).

72. T. E. Madey, Sur. Sci., 23, 355 (1972).

73. K. Kraemer and D. Menzel, Ber. Bun. Ges., 78, 591 (1974).

74. D. O. Hayward and B. M. W. Trapnell, Chemisorption, ch. 3 (Butterworths and Company (Publishers), Ltd., London, 1964).

75. C. W. Tucker, J. App. Phys., 37, 528 (1966).

76. C. W. Tucker and C. B. Duke, Sur. Sci., 29, 237 (1972).

77. C. W. Tucker, J. App. Phys., 37, 4147 (1966).

78. C. W. Tucker, J. App. Phys., 38, 2696 (1967).

79. G. W. Simmons, D. F. Mitchell and K. R. Lawless, Sur. Sci., 8, 130 (1967).

80. J. W. May and L. H. Germer, Sur. Sci., 11, 443 (1968).

81. K. S. Kim and N. Winograd, J. Catal., 35, 66 (1974).

82. P. R. Norton and R. L. Tapping, Faraday Disc. of Chem. Soc., 60, 71 (1975).

83. R. Ducros and R. P. Merrill, Sur. Sci., 55, 227 (1976).

84. V. P. Ivanov, G. K. Boreshow, V. I. Savchenko, W. F. Egelhoff and W. H. Weinberg, to be published.

85. C. R. Helms, H. P. Bonzel and S. Kelemen, J. Chem. Phys., 65, 1773 (1976).